

The role of advance ratio and aspect ratio in determining leading-edge vortex stability for flapping flight

R. R. Harbig, J. Sheridan[†] and M. C. Thompson

Fluids Laboratory for Aeronautical and Industrial Research (FLAIR), Department of Mechanical and Aerospace Engineering, Monash University, Clayton, VIC 3800, Australia

(Received 18 November 2013; revised 4 April 2014; accepted 6 May 2014)

The effects of advance ratio and the wing's aspect ratio on the structure of the leading-edge vortex (LEV) that forms on flapping and rotating wings under insect-like flight conditions are not well understood. However, recent studies have indicated that they could play a role in determining the stable attachment of the LEV. In this study, a numerical model of a flapping wing at insect Reynolds numbers is used to explore the effects of these parameters on the characteristics and stability of the LEV. The word 'stability' is used here to describe whether the LEV was attached throughout the stroke or if it was shed. It is demonstrated that increasing the advance ratio enhances vorticity production at the leading edge during the downstroke, and this results in more rapid growth of the LEV for non-zero advance ratios. Increasing the wing aspect ratio was found to have the effect of shortening the wing's chord length relative to the LEV's size. These two effects combined determine the stability of the LEV. For high advance ratios and large aspect ratios, the LEV was observed to quickly grow to envelop the entire wing during the early stages of the downstroke. Continued rotation of the wing resulted in the LEV being eventually shed as part of a vortex loop that peels away from the wing's tip. The shedding of the LEV for high-aspect-ratio wings at non-zero advance ratios leads to reduced aerodynamic performance of these wings, which helps to explain why a number of insect species have evolved to have low-aspect-ratio wings.

Key words: biological fluid dynamics, swimming/flying, vortex shedding

1. Introduction

Current interest in developing micro-air-vehicles (MAVs) has motivated significant research into the aerodynamics of flapping and rotating wings in an attempt to understand the mechanisms that insects and birds use to fly. Research into the aerodynamics of insect flight has revealed that insects employ a number of unsteady mechanisms. These include delayed stall (Ellington *et al.* 1996), rapid pitch rotation (Dickinson, Lehmann & Sane 1999), wake capture (Dickinson *et al.* 1999) and clap and fling (Weis-Fogh 1973). However, the delayed stall mechanism, associated with

[†] Email address for correspondence: john.sheridan@monash.edu

the formation of a coherent leading-edge vortex (LEV), is regarded as being primarily responsible for the elevated lift coefficients that are required for insect flight (Sane 2003).

For hovering flight, the LEV forms at the beginning of each half-stroke and remains attached to the wing throughout the half-stroke (Ellington *et al.* 1996). This stable attachment provides the wing with additional circulation and enhanced lift (Ellington *et al.* 1996; Usherwood & Ellington 2002; Birch, Dickson & Dickinson 2004). Owing to the wing's rotation, the LEV is three-dimensional in structure and is often accompanied by a strong spanwise flow that acts from the wing root to tip (Birch & Dickinson 2001; Birch *et al.* 2004; Poelma, Dickson & Dickinson 2006). The attachment of the LEV throughout a half-stroke is essential for the wing's performance, but the mechanism that stabilises the LEV is not well understood. Here the word 'stable' and its derivatives are used to describe whether the LEV remains attached throughout the stroke (stable) or if it is shed (unstable), as it is commonly used in the flapping wing literature (e.g. Ellington *et al.* 1996; Lentink & Dickinson 2009; Shyy *et al.* 2010). It is not to be confused with 'flow stability' in the classical sense that relates to the growth or decay of perturbations. Some studies have suggested that the spanwise flow stabilises the LEV by draining vorticity generated at the leading edge into the tip vortex (Maxworthy 1979; Ellington *et al.* 1996; van den Berg & Ellington 1997). However, for a translating wing at insect Reynolds numbers, generating a spanwise velocity through wing sweep alone is not sufficient to maintain an attached LEV (Lentink & Dickinson 2009; Beem, Rival & Triantafyllou 2012). Curiously though, wing sweep on a rotating wing can be used to modulate the LEV strength and possibly its stability (Rival & Wong 2013; Wong, Kriegseis & Rival 2013). Birch & Dickinson (2001) and Cheng *et al.* (2013) have suggested that it is the downwash velocity that is created by the tip vortex and wake vorticity that stabilises the LEV, as it limits the strength of the LEV by convecting and tilting vorticity into other components. Finally, the stability of the LEV has been related to the wing's rotation, as the LEV is unstable for a two-dimensional translating wing (Dickinson & Gotz 1993) but is stable for a revolving wing (Lentink & Dickinson 2009). Thus, Lentink & Dickinson (2009) have proposed that it is the low-Rossby-number (Ro) propeller-like rotation of the wing that stabilises the LEV, owing to the large rotational accelerations that are produced.

The low-Rossby-number hypothesis of Lentink & Dickinson (2009) suggests that the LEV would become unstable at some point under forward flight conditions (high Rossby numbers). However, the change in the LEV's characteristics with flight speed is not well understood. Ellington (1984b) used the advance ratio (J) to define the flight speed of an insect relative to its wing-tip flapping velocity. Ellington (1999) reported that, as the advance ratio increases, the downstroke increasingly dominates the force balance owing to the increased relative velocity seen by the wing. Dickson & Dickinson (2004) investigated this further by measuring the aerodynamic forces on a wing that combined a revolving motion with a uniform free-stream velocity that acted in the plane of the wing's rotation. They showed that the aerodynamic forces are non-constant for non-zero advance ratios, where they varied with both the advance ratio and the wing's rotation angle. They suggested that this variation in aerodynamic forces could be characterised by a single variable (at a constant angle of attack), the tip velocity ratio. Nagai *et al.* (2009) conducted both numerical and experimental investigations into the effect of advance ratio using a flapping bumblebee wing, whose stroke plane was set at 45° to a uniform free-stream flow. They found a similar variation in lift and drag coefficients as Dickson & Dickinson (2004)

and demonstrated that at mid-downstroke the LEV was larger for higher advance ratios, but remained attached to the wing for all the advance ratios that were tested. Conversely, the LEV was smaller during the upstroke for increasing advance ratios and only formed on the outer part of the wing as a result of the locally reversed flow in the inner part of the wing. Bross, Ozen & Rockwell (2013) undertook a particle image velocimetry (PIV) experiment on a rotating wing in a uniform free-stream flow that was perpendicular to the wing's rotation plane. They found that, if the effective angle of attack is matched, then similar LEV structures are generated over a range of advance ratios.

The low-Rossby-number hypothesis also linked the wing's aspect ratio to the LEV's stability, as the Rossby number equalled the aspect ratio for hovering flight (Lentink & Dickinson 2009). This indicated that the LEV could become unstable for high-aspect-ratio wings. However, in a previous study we demonstrated that the LEV remained attached over a range of wing aspect ratios under hovering flight conditions and that similar LEV structures could be produced if the flow field is scaled using the wing's span (Harbig, Sheridan & Thompson 2013). This scaling results in a span-based Reynolds number (Re_R) and Rossby number. While this study showed that the wing's aspect ratio does not influence LEV stability for hovering flight, it is still possible that the LEV could become unstable at higher advance ratios. Therefore, an investigation into the effect of aspect ratio at non-zero advance ratios is required.

This paper describes an investigation into the effect of aspect ratio and advance ratio on the characteristics and stability of the LEV for flapping wings at insect Reynolds numbers. A numerical model of a fruit-fly wing undergoing a simplified flapping motion is first presented and the time evolution of the LEV structure throughout a flapping cycle under hovering conditions is highlighted. The changes in the characteristics of the LEV with advance ratio are then explored at a span-based Reynolds number of 613, with particular emphasis being given to the downstroke. This model is extended to wings of different aspect ratio, and the effect of advance ratio and aspect ratio on the stability of the LEV is discussed. The effects of advance ratio and aspect ratio at a span-based Reynolds number of 7668 are also investigated, and it is shown that stability of the LEV is still dependent on these parameters at this Reynolds number. Finally, the results of our study are discussed in relation to LEV stability theories.

2. Numerical method

The flow over a flapping wing is modelled by the Navier–Stokes equations cast in a non-inertial rotating frame of reference and combined with the continuity constraint. In order to minimise numerical error, the ‘alternate rotation model’ was used, whereby the velocity in the advection and transient terms of the momentum equation was modified to involve the absolute frame velocity rather than the relative frame velocity. The equations that were solved were written in the form

$$\frac{\partial \rho \mathbf{u}_{abs}}{\partial t} + \nabla \cdot (\rho \mathbf{u} \mathbf{u}_{abs}) = -\nabla p + \nabla \cdot \boldsymbol{\tau} - \rho \boldsymbol{\Omega} \times \mathbf{u} - \rho \boldsymbol{\Omega} \times (\boldsymbol{\Omega} \times \mathbf{r}) \quad (2.1)$$

and

$$\nabla \cdot \mathbf{u} = 0. \quad (2.2)$$

Here, ρ is the fluid density, \mathbf{u} and \mathbf{u}_{abs} are the velocity vectors in the rotating and absolute frames, respectively, p is the pressure, $\boldsymbol{\Omega}$ is the rotational velocity vector, \mathbf{r} is the location vector and $\boldsymbol{\tau}$ is the stress tensor, which is defined as

$$\boldsymbol{\tau} = \mu(\nabla \mathbf{u} + (\nabla \mathbf{u})^T - \frac{2}{3} \mathbf{I} \nabla \cdot \mathbf{u}), \quad (2.3)$$

with μ the fluid viscosity and \mathbf{I} the identity matrix. The angular acceleration of the fluid is included in the transient term as $\mathbf{u}_{abs} = \mathbf{u} + \boldsymbol{\Omega} \times \mathbf{r}$, and the Coriolis and centrifugal terms are the last two terms, respectively, in (2.1). These equations were solved directly using the commercial finite-volume-based code ANSYS CFX. The formally second-order-accurate specified blend factor scheme (with $\beta = 1$) was used for spatial discretisation, and a second-order backward Euler scheme for the time evolution terms.

2.1. Geometry and kinematics

The wing was modelled as a rigid plate with square edges with a thickness of 3% of the mean chord and the planform shape was based on a generic fruit-fly wing (*Drosophila melanogaster*). The wing was scaled to have a wing span of 2.47 mm and an aspect ratio of 2.91, similar to that of an actual fly's wing (Zanker 1990). This wing shape was stretched to produce wings of different aspect ratios between 2.91 and 7.28 to reflect the variety seen in nature (for examples, see Ellington (1984a) and Shyy *et al.* (2010)). An example of the fruit-fly wing is presented in figure 1, as well as the coordinate system used in this model.

In this study a 'normal hovering' (Weis-Fogh 1973) type of kinematics was used as a simplification of a real insect's flapping stroke, where the wing's stroke plane is horizontal. The wing's motion can be described by the temporal variation of two kinematic angles: the stroke position angle $\phi(t)$, and the angle of incidence $\alpha_i(t)$. These angles are depicted in figure 1, where the stroke position angle is the angle between the z -axis and the mid-stroke line, and the angle of incidence is the angle between the wing's chord line and the stroke plane's normal vector (y -axis). Figure 2(a) shows the temporal variation of these two kinematic angles over the first 1.25 cycles. A dimensionless time (t^*) is also defined that varies between zero and one for each flapping cycle, where the upstroke is between $0 \leq t^* \leq 0.5$ and the downstroke is between $0.5 \leq t^* \leq 1$. A schematic of the wing's motion is also shown in figure 2(b), which highlights the relative motion of the wing for the up- and downstrokes compared to the free-stream velocity V . Insects that use this type of flapping kinematics for hovering flight typically tilt their wing's stroke plane in order to produce thrust to achieve forward flight (e.g. Dudley & Ellington 1990; Willmott & Ellington 1997). The amount of stroke plane tilt that is required at a particular flight speed depends on the thrust that is required to overcome the insect's body drag, and can be quite large for high advance ratios. Additionally, under these forward flight conditions, the wing's angle of attack is no longer constant along the wing's span due to the component of free-stream velocity that acts normal to the stroke plane. Insects also adjust their wing's pitch angle kinematics to fit the advance ratio and stroke plane angle (Ellington 1999; Sun 2003). The degree to which the wing's angle of attack and stroke plane angle vary with advance ratio depends on the insect. As this study was of a more general nature, a simplification was made whereby all simulations were run with a horizontal stroke plane and constant wing kinematics, regardless of the advance ratio. This was done to simplify the analysis, as it allowed a constant stroke plane angle with advance ratio and for the wing's angle of attack to remain constant between advance ratios and along the wing's span.

The wing's kinematics consisted of a rotation about its base (y -axis), where the wing's stroke position $\phi(t)$ followed a smoothed triangular motion (see figure 2). A smoothed triangular motion has been used previously to simulate a fruit-fly's hovering stroke (Sane & Dickinson 2001; Poelma *et al.* 2006) and allowed a more direct comparison to a previously reported impulsively started rotating wing model

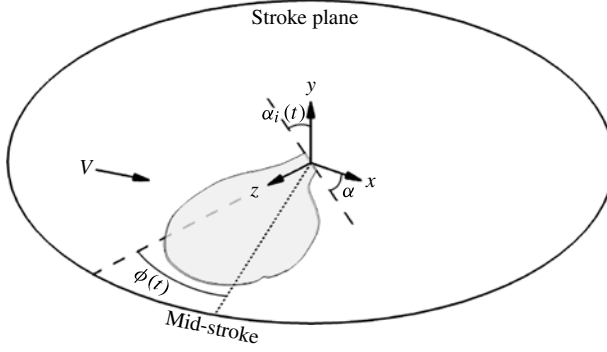


FIGURE 1. Schematic of fly wing geometry, kinematic angles and coordinate system. The origin of the coordinate system is located at the wing's root. The coordinate system rotates with the wing's stroke position (about the y -axis), but not the wing's pitch rotation (z -axis). Thus the zx -plane defines the wing's stroke plane, with the z -axis aligned with the wing's span and the y -axis points vertically.

(Harbig *et al.* 2013) than a sinusoidal motion. The wing's stroke position was described by (2.4), where t is the time from mid-downstroke,

$$\phi(t) = \begin{cases} -\Omega t, & t \leq \frac{T}{4} - t_r, \\ 2t_r \left(\Omega t_1^2 - \Omega t_1 + \frac{\Omega}{2\pi^2} \cos(2\pi t_1') \right) - \Omega \left(\frac{T}{4} - t_r + \frac{t_r}{\pi^2} \right), & \frac{T}{4} - t_r < t < \frac{T}{4} + t_r, \\ \Omega t - \Omega \frac{T}{2}, & \frac{T}{4} + t_r \leq t \leq \frac{3T}{4} - t_r, \\ -2t_r \left(\Omega t_2^2 - \Omega t_2 + \frac{\Omega}{2\pi^2} \cos(2\pi t_2') \right) + \Omega \left(\frac{T}{4} - t_r + \frac{t_r}{\pi^2} \right), & \frac{3T}{4} - t_r < t < \frac{3T}{4} + t_r, \\ -\Omega t + \Omega T, & t \geq \frac{3T}{4} + t_r, \end{cases} \quad (2.4)$$

where

$$t_1' = \frac{t - \frac{1}{4}T + t_r}{2t_r} \quad (2.5)$$

and

$$t_2' = \frac{t - \frac{3}{4}T + t_r}{2t_r}. \quad (2.6)$$

The constant rotational velocity of the wing (Ω) during the up- and downstroke is dependent on the peak-to-peak amplitude (Φ) of the wing's stroke and can be calculated by the function $\Omega = \Phi / (T/2 - t_r + 4t_r/\pi^2)$, where T is the period of a flapping cycle and t_r is half the stroke reversal time, i.e. around stroke reversal the function is smoothed over a period of $2t_r$. In order to completely define $\phi(t)$, values for the flapping frequency n , peak-to-peak amplitude and stroke reversal time are required. Values of $n = 218$ Hz and $\Phi = 140^\circ$ were chosen and are representative of a real fruit-fly's kinematics (Fry, Sayaman & Dickinson 2005). A stroke reversal time of 16% of the flapping period was used, i.e. $2t_r = 0.16T$.

The wing's angle of incidence $\alpha_i(t)$ varied according to a smoothed trapezoidal motion (see figure 2). Note that for clarity $\alpha_i(t)$ is not the wing angle of attack α .

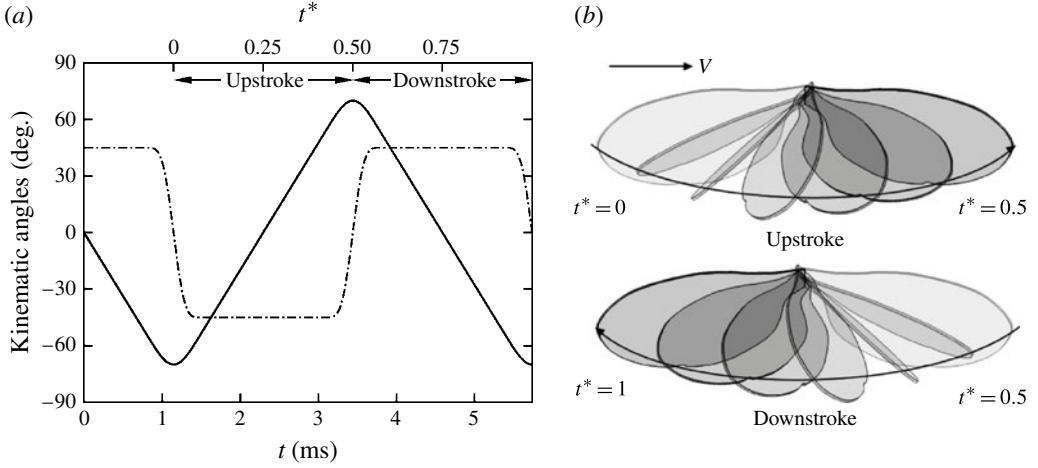


FIGURE 2. Wing kinematics plots. (a) Time variation of kinematic angles for the first 1.25 cycles. Dimensionless time (t^*) is also shown at the top, where $t^* = 0$ at the beginning of the upstroke. Solid line is the stroke position angle $\phi(t)$ and dashed line is the angle of incidence $\alpha_i(t)$. (b) Schematic of the wing's motion and free-stream velocity (V).

The time variation of $\alpha_i(t)$ is described by

$$\alpha_i(t) = \begin{cases} 90 - \alpha_0, & t \leq \frac{T}{4} - t_r, \\ \frac{4(90 - \alpha_0)}{3\pi} \sin(2\pi t'_1) - 2(90 - \alpha_0)t'_1 \\ \quad - \frac{90 - \alpha_0}{6\pi} \sin(4\pi t'_1) + 90 - \alpha_0, & \frac{T}{4} - t_r < t < \frac{T}{4} + t_r, \\ -(90 - \alpha_0), & \frac{T}{4} + t_r \leq t \leq \frac{3T}{4} - t_r, \\ -\frac{4(90 - \alpha_0)}{3\pi} \sin(2\pi t'_2) + 2(90 - \alpha_0)t'_2, \\ \quad + \frac{90 - \alpha_0}{6\pi} \sin(4\pi t'_2) - (90 - \alpha_0), & \frac{3T}{4} - t_r < t < \frac{3T}{4} + t_r, \\ 90 - \alpha_0, & t \geq \frac{3T}{4} + t_r, \end{cases} \quad (2.7)$$

where α_0 is the angle of attack at mid-downstroke and was equal to 45° , t'_1 and t'_2 are given by (2.5) and (2.6), respectively, and t_r is half the flip reversal time. Equation (2.7) was written such that the wing's pitch rotation occurred symmetrically around stroke reversal and $2t_r$ was set to 16% of the flapping period so that the duration of the wing's flip occurred over the same period as stroke reversal. The wing's pitch rotation axis was the z -axis, which was located at 21.5% of the wing's maximum chord referenced from the leading edge.

In an earlier study we demonstrated that, by scaling the flow using the wing's span as the characteristic length, Reynolds-number effects can be decoupled from aspect-ratio effects when comparing results between differently shaped wings (Harbig *et al.* 2013). Therefore, this scaling is adopted here and the Reynolds number was calculated using the average velocity at the wing tip (\bar{U}_{tip}) and the wing's span (R).

This Reynolds number represents an approximate average over the entire flapping cycle, as the effect of the free-stream velocity V on \bar{U}_{tip} over a complete flapping cycle averages out to zero. Two span-based Reynolds numbers, of 613 and 7668, were considered in this study, which correspond to fruit-fly and house-fly scales, respectively. Changing the Reynolds number between simulations was achieved by altering the fluid's viscosity.

Owing to the change in the relative velocity experienced by the wing at non-zero advance ratios (see § 3.2.1), the ‘instantaneous’ Reynolds number varies throughout a flapping cycle. The variation in Reynolds number is equal to $\pm JRe_R$, where Re_R is the time-averaged Reynolds number as described above. Thus, the higher the advance ratio, the larger the change in instantaneous Reynolds number over the cycle. This variation in instantaneous Reynolds number will occur on a real insect as it increases its flight speed and therefore it is a natural part of the problem. Other studies have shown that there are Reynolds-number effects within this range (e.g. Birch *et al.* 2004; Aono, Liang & Liu 2008). These Reynolds-number effects can be observed in our results, but they appear to be minor compared to other effects that advance ratio has on the flow structures, which will be discussed below.

The advance ratio is defined as $J = V/(2\Phi nR)$ (Ellington 1984b), which is the ratio of the insect's flight speed to the average velocity at the wing's tip due to its rotation. The free-stream velocity was perpendicular to the mid-stroke line (see figure 1) and was adjusted to achieve the desired advance ratio. The wing was initially at rest in quiescent fluid. At the start of the simulation the free-stream velocity was applied to the domain boundary (see § 2.2) and the wing's motion was started from mid-downstroke. The simulation was run for four complete flapping cycles. Comparison of the aerodynamic forces between the third and fourth cycles showed an average variation of only 2.8%. Therefore the solution was deemed to have stabilised and the results of the fourth cycle were recorded.

2.2. Domain set-up

Two computational domains were employed to construct the flow field for this model, an outer ‘stationary’ domain and an inner ‘rotating’ domain (see figure 3). The outer domain consisted of a cube with sides of 18 times the wing's span in length. In this domain, the Navier–Stokes equations were solved in an inertial frame that moved at the insect's flight speed V , i.e. (2.1) and (2.2) with the rotational terms removed and where $\mathbf{u} = \mathbf{u}_{abs}$. The stationary domain was aligned with the free-stream flow such that four of the faces were parallel to the free stream and two were perpendicular. The parallel faces were assigned free-slip wall boundary conditions ($U_n = 0$), while the free-stream velocity was prescribed uniformly across the upstream face and the average pressure across the downstream boundary was set to zero gauge pressure. These boundary conditions were applied when $J > 0$; however, for the hovering simulations, when $J = 0$, the fluid was allowed to flow into or out of all six faces with the average pressure across each boundary set to zero gauge pressure.

The rotating domain was spherical in shape, with a diameter seven times the wing's span, and was located in the centre of the stationary domain. The wing was located in this domain such that its base was situated on the centre point of the domain. This domain rotated about the wing's rotation axis (y -axis) according to (2.4), and as such the fluid dynamic equations were solved in a non-inertial rotating frame of reference ((2.1) and (2.2)). A no-slip boundary condition was applied on the wing's surface and a general grid interface (GGI) connection was applied between the rotating

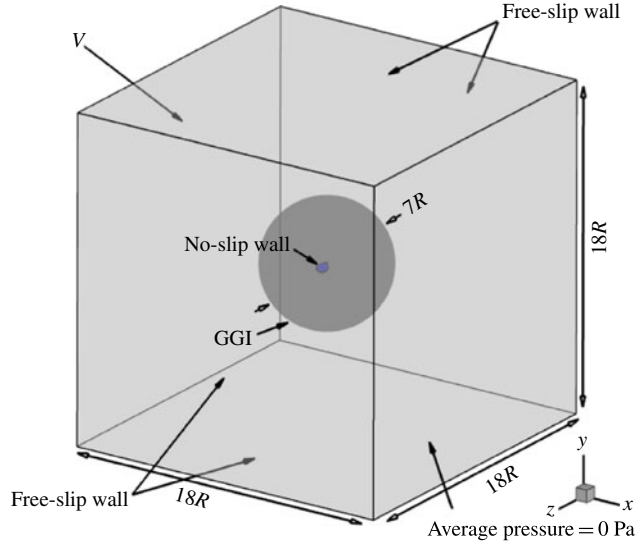


FIGURE 3. (Colour online) Computational domain and imposed boundary conditions for when $J > 0$. When $J = 0$ the boundary condition on all six outer faces is an average pressure of zero gauge pressure. The stationary domain is shown in light grey, the rotating domain is in grey and the wing is in dark grey (blue online).

and stationary domains to allow fluid flow between the two. The GGI connection uses a physically based intersection algorithm to connect the grid topology across the interface. A control surface approach is then applied to perform the connection. By using this approach, strict conservation is maintained of the surface fluxes (mass, momentum, energy, etc.) for all equations across the interface.

The stationary and rotating domains were meshed using an unstructured tetrahedral mesh with a region of triangular prism elements near the wing's surface to resolve the velocity gradients in this area. This boundary-layer mesh was generated using 23 layers with a growth rate of 1.2 and a maximum thickness of $0.12\bar{c}$, where \bar{c} is the wing's mean chord length. The rotating domain was constructed using two non-conformal mesh regions that consisted of a smaller sphere of diameter 3.5 times the wing's span concentrically located inside the larger sphere. The mesh inside the small sphere was fixed to the wing and was allowed to rotate about the wing's spanwise axis (z -axis) according to (2.7). Thus an additional GGI connection was applied on the interface of the large and small spheres to enable the sliding mesh interface.

2.3. Validation

Mesh and time-step resolution studies were conducted to ensure that numerical errors were below an acceptable level. The grid convergence index (GCI) method (Roache 1998) was used to estimate the level of numerical error. These validation studies were performed using the fruit-fly wing ($AR = 2.91$) at a span-based Reynolds number of 7668 and for an advance ratio of zero. Mesh resolution was explored using three grids that were generated by halving the element size on the wing's surface and in the surrounding fluid zones. The flow field was calculated on each mesh and the variation of the lift and drag coefficients throughout the fourth flapping cycle were compared. The average relative error ($\bar{\epsilon}$) over the flapping cycle was used to calculate the GCI

Mesh	Surface size	Elements (million)	C_L		C_D	
			$\bar{\epsilon}$	GCI (%)	$\bar{\epsilon}$	GCI (%)
3	0.02857 \bar{c}	4.099	—	9.27	—	10.6
2	0.01449 \bar{c}	9.991	0.0339	5.04	0.0336	6.41
1	0.00725 \bar{c}	49.26	0.0268	1.69	0.0305	2.60

TABLE 1. Mesh resolution study at $Re_R = 7668$.

and was computed from

$$\bar{\epsilon} = \frac{1}{m} \sum_{i=1}^m \left(\frac{f_2 - f_1}{f_1} \right)_i, \quad (2.8)$$

where m is the number of time steps per cycle, and f_2 and f_1 are the solution values at time step i on the coarse and fine grids, respectively. The average relative error and corresponding GCI values for both the lift and drag coefficients are shown in table 1. The GCI was found to be 2.6% for mesh 1. This mesh offered a significant improvement in numerical error over the intermediate mesh and was therefore selected for this study. A similar approach was used for the time-step resolution study whereby the simulation was run three times and each time the time step was halved. This yielded a GCI of 2% using a time step of $\Delta t = T/(4\Phi)$.

With the grid and time-step sizes selected, a simulation with slightly different kinematics was constructed in order to compare our numerical results to the experimental force measurements of Sane & Dickinson (2001). Sane & Dickinson (2001) used a dynamically scaled model of a fruit-fly wing to study how changes in wing kinematics influence the aerodynamic forces acting on the wing throughout the flapping cycle. A set of these experimental results was used as a point of comparison to validate the numerical model. The kinematics consisted of a smoothed triangular motion for the wing's stroke position and a smoothed trapezoidal motion for the wing's angle of incidence with a flip duration of 16% of the flapping period. The peak-to-peak amplitude was 180° and the angle of attack of the wing at mid-stroke was 50°.

Sane & Dickinson (2001) did not specify an exact Reynolds number for this experiment, as it varied between the different kinematic motions considered; however, they stated that it was in the range of 100. Nonetheless, we estimated the Reynolds number, based on the mean wing chord length, to be 110 using their wing's geometry and fluid's kinematic viscosity for this particular set of kinematics. This Reynolds number was matched in the computational model.

The comparison between the experimental and numerical lift and drag coefficients over the flapping cycle is shown in figure 4. The lift and drag coefficients were calculated as $C_L = 2L/(\rho \bar{U}_{rg}^2 S)$ and $C_D = 2D/(\rho \bar{U}_{rg}^2 S)$, respectively, where S is the wing area, L is the aerodynamic force acting in the y -direction and D is the force opposing the wing's rotation in the zx -plane. The aerodynamic forces are plotted as a function of dimensionless time (t^*) from the beginning of the upstroke. Note that Sane & Dickinson (2001) estimated the contribution of added mass to their force measurements and found that added-mass effects were only a small proportion of the net aerodynamic force. Furthermore, they decided that both added-mass and aerodynamic contributions are biologically relevant, and therefore chose not to subtract the added-mass estimates from the measured force traces. The experimental

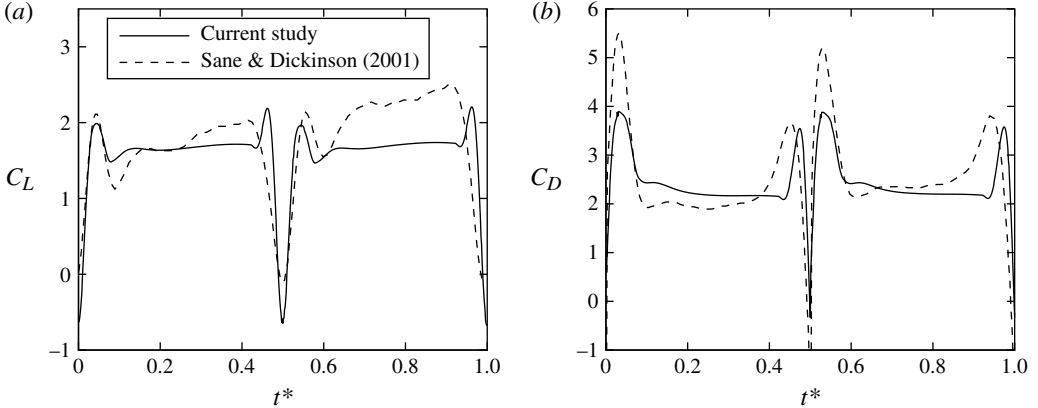


FIGURE 4. Variation of the lift and drag coefficients over a flapping cycle ($\Phi = 180$, $\alpha_0 = 50^\circ$, $Re_c = 110$). Comparison of the current study with the experimental results of Sane & Dickinson (2001).

data shown in figure 4 therefore include added-mass effects. The numerical data also have added-mass effects, and, because the wing is geometrically similar and is undergoing an identical flapping motion, the added-mass effects will be comparable between the experimental and numerical data.

Both the experiment and the numerical model were performed in hovering conditions, and therefore the variation in aerodynamic forces is symmetric for both the upstroke ($0 \leq t^* \leq 0.5$) and downstroke ($0.5 \leq t^* \leq 1.0$) for the numerical simulations. Some asymmetry can be observed in the experimental results, particularly in the lift coefficient measurements, which Sane & Dickinson (2001) suggest is due to ‘small asymmetries in the stroke pattern introduced by the gearbox of the model’. Overall, better agreement is seen between the numerical and experimental results for the upstroke, where the average lift coefficient is 1.81 % lower and the drag coefficient is 0.38 % higher than the experimental values. This is compared to 17.43 and 7.12 % lower for the mean lift and drag coefficients, respectively, for the downstroke. Nonetheless, the variation in the aerodynamic forces is consistent throughout the cycle. The peaks in aerodynamic forces, both before and after each stroke reversal due to rapid pitch rotation and wake capture, respectively, are clearly seen in the numerical data. The timing of the force peak after stroke reversal, associated with wake capture, is in good agreement with the experimental results. However, the rapid pitch rotation force peak is slightly delayed compared to the experimental results. This suggests that there may be a difference in kinematics in this portion of the flapping cycle in which the experimental wing begins its pitch rotation earlier in the cycle compared to the numerical model.

3. Results at low Reynolds number

3.1. Hovering

A number of studies have investigated the vortex structures that form over a flapping wing under hovering conditions (e.g. Poelma *et al.* 2006; Aono *et al.* 2008; Liu & Aono 2009; Jardin, Farcy & David 2012). The change in flow structures over the wing throughout the downstroke for our simulations at zero advance ratio is shown in figure 5 (also see supplementary movie 1 available at

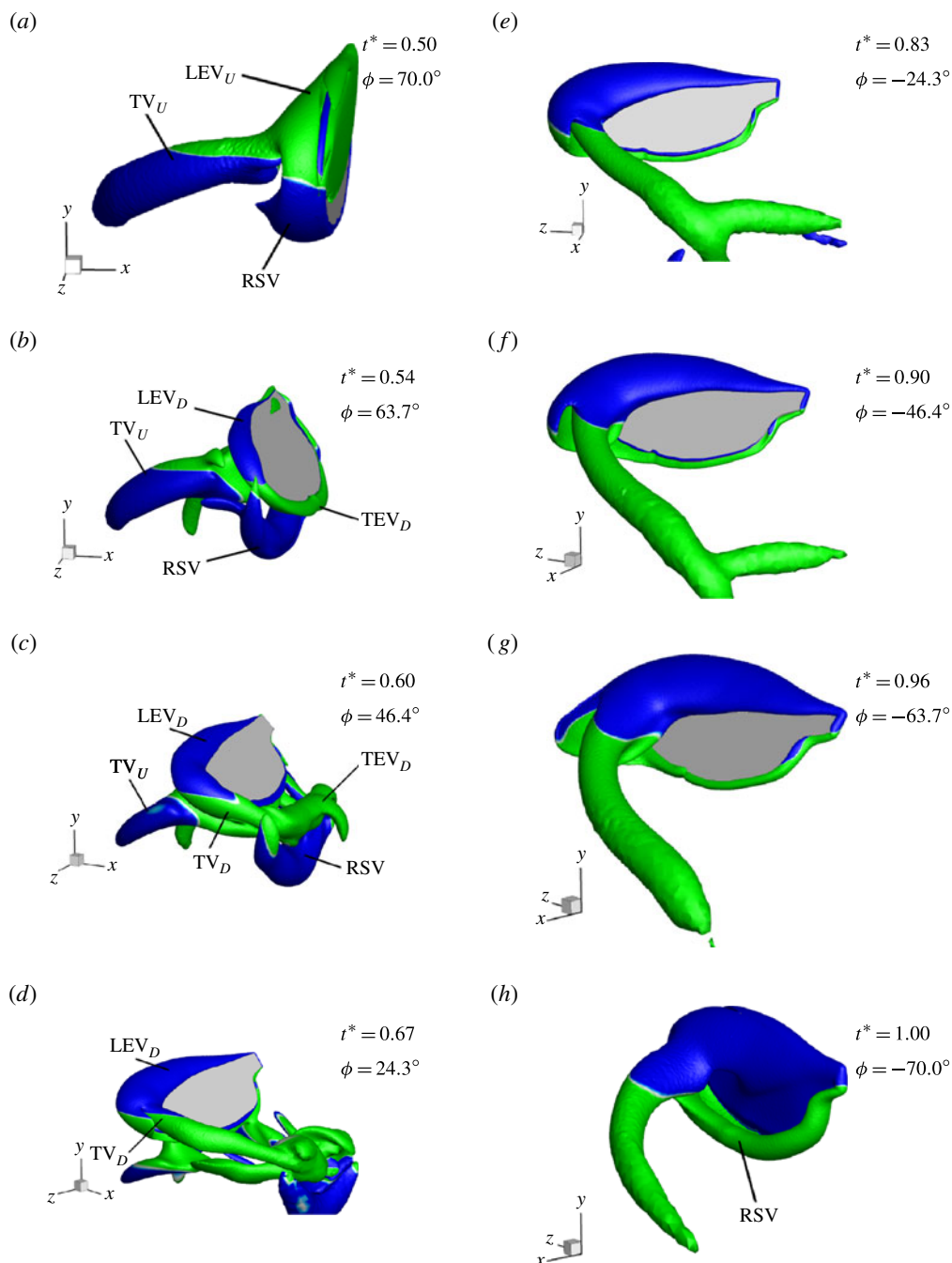


FIGURE 5. (Colour online) Stationary view of the wing's motion (clockwise rotation) and the generated flow structures during the downstroke for hovering conditions ($J=0$, $AR=2.91$, $Re_R=613$). Vortex structures are visualised by iso- Q surfaces shaded (coloured online) by spanwise vorticity to indicate direction: mid grey (green online) is positive and dark grey (blue online) is negative. The sequence progresses from (a) to (h). See also supplementary movie 1.

<http://dx.doi.org/10.1017/jfm.2014.262>). The vortex structures are visualised using iso-surfaces of Q criterion, which is the second invariant of the velocity gradient tensor (Hunt, Wray & Moin 1988). The Q criterion is a measure of the magnitude of rotation rate relative to strain rate in a fluid. Positive values of Q represent areas where the local magnitude of rotation in the fluid dominates relative to strain and therefore can be used to highlight vortical structures. The formation of flow structures observed here is comparable to that reported in these earlier studies, and, owing to the symmetric flapping kinematics, this flow pattern is repeated for the upstroke but with the vortex structures having opposite directions of rotation.

At the beginning of the downstroke ($t^* = 0.5$), the LEV_U and tip vortex (TV_U) system from the previous upstroke can be seen, along with the rotational starting vortex (RSV) that is created by the pitch rotation of the wing. This RSV is shed from the wing as it continues its pitch rotation and the LEV_U is also shed as the wing reverses its direction ($t^* = 0.54$). At this point, a horseshoe-shaped vortex is formed around the wing comprising a new LEV_D , TV_D and trailing-edge vortex (TEV_D). As the wing's motion continues, this horseshoe vortex grows in size, particularly towards the wing's tip, which results in a conically shaped LEV. The previously shed LEV_U and TV_U from the upstroke are swept underneath the wing and the newly formed TEV_D is shed from the wing ($t^* = 0.6$). These vortex structures are left behind in the wake of the wing as it continues to rotate. From about $t^* \approx 0.83$ the flow structures on the wing remain more or less steady until the wing begins its pitch up at the end of the stroke, at which point a new RSV is created at the trailing edge.

3.2. Effect of advance ratio

3.2.1. Aerodynamic forces

The effect of advance ratio is generally to create an asymmetry between the upstroke and the downstroke. This can be seen in both the aerodynamic forces and flow structures that are generated for each half-stroke. This asymmetry is induced by the change in relative velocity experienced by the wing, where the relative velocity is increased during the downstroke but is reduced for the upstroke (Dickson & Dickinson 2004). Increasing the advance ratio increases this imbalance and thus for high advance ratios the aerodynamic forces are much larger for the downstroke compared to the upstroke (Ellington 1999; Dickson & Dickinson 2004; Nagai *et al.* 2009). This can be seen in figure 6, which shows the variation in lift and drag coefficients throughout the cycle at $J = 0, 0.25$ and 0.5 . The aerodynamic force coefficients are reduced during the upstroke ($0 \leq t^* \leq 0.5$) but are augmented during the downstroke ($0.5 \leq t^* \leq 1.0$) for increasing advance ratio. Note that the coefficients here are calculated using the average flapping velocity at the radius of gyration (\bar{U}_{rg}), and therefore the effect of the free-stream velocity is not incorporated into the calculation of the coefficients, as it averages out to zero over a complete flapping cycle.

Nagai *et al.* (2009) reported that advance ratio changes the effectiveness of the pitch rotation and wake capture mechanisms, which can also be seen in our simulations. Outside of these stroke reversal periods, the wing produces approximately constant lift and drag coefficients under hovering conditions ($J = 0$). For non-zero advance ratios, the aerodynamic forces are no longer constant and vary throughout each half-stroke such that there is a minimum around mid-upstroke and a maximum around mid-downstroke. This was first observed by Dickson & Dickinson (2004) in their rotating wing experiments where they demonstrated that the aerodynamic forces depended on both the advance ratio and the wing's stroke position.

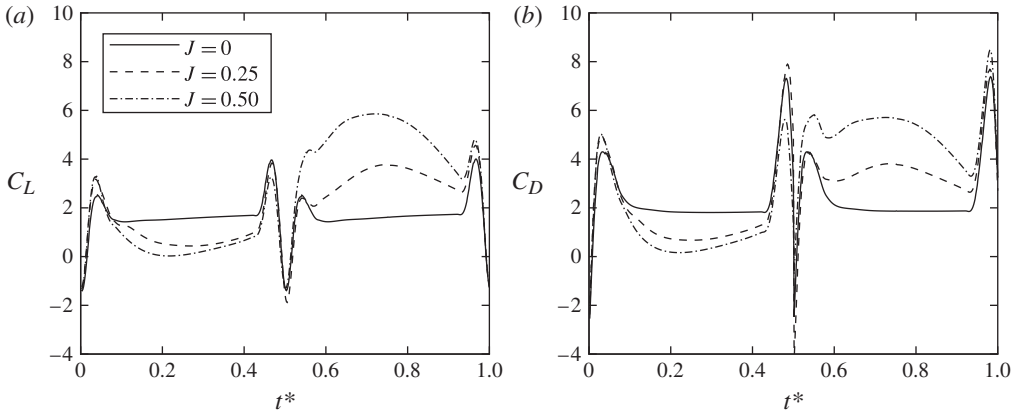


FIGURE 6. Change in lift and drag coefficients throughout a flapping cycle with advance ratio. Results are for the $AR=2.91$ wing at $Re_R=613$ and the lift and drag coefficients are based on average flapping velocity at the radius of gyration (\bar{U}_{rg}).

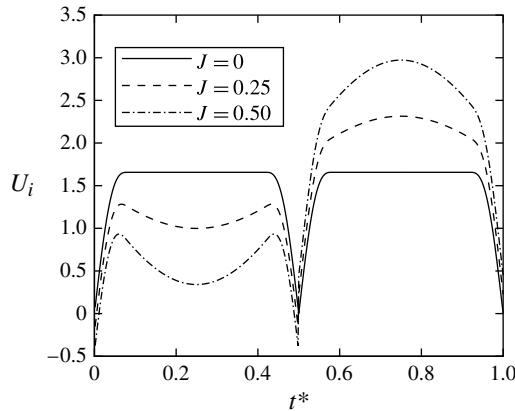


FIGURE 7. Time variation of the relative velocity at the wing's radius of gyration throughout a flapping cycle for different advance ratios.

Dickson & Dickinson (2004) suggested that the variation in aerodynamic forces could be accounted for by using the wing-tip velocity ratio, which they defined as the ratio of the chordwise components of flow velocity at the wing tip due to translation and revolution. The tip velocity ratio varies between $-J$ at mid-upstroke and J at mid-downstroke. Using this ratio in the calculation of the lift and drag coefficients effectively computes a force coefficient that is based on the instantaneous relative velocity seen by the wing. For our simulations, the time variation in relative velocity at a particular spanwise location (r) is given by $U_i = r|d\phi(t)/dt| \pm V \cos \phi(t)$, where the two velocity components are added together for the downstroke and are subtracted for the upstroke. The variation in this velocity throughout the wing's stroke for different advance ratios is presented in figure 7. The U_i value is positive when the velocity is in the opposite direction to the wing's motion. Increasing the advance ratio results in higher relative velocities experienced by the wing during the downstroke

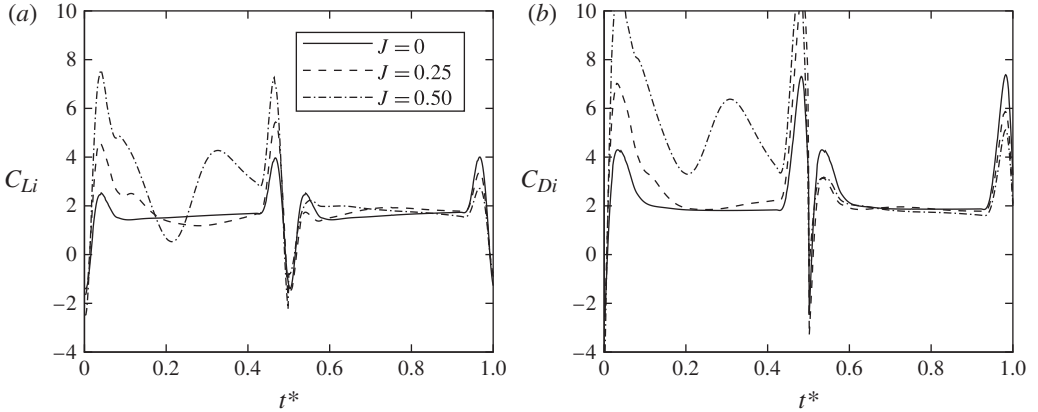


FIGURE 8. Change in instantaneous lift and drag coefficients throughout a flapping cycle with advance ratio. Results are for the $AR=2.91$ wing at $Re_R=613$ and the lift and drag coefficients are calculated using the instantaneous velocity at the radius of gyration (U_i).

and lower velocities for the upstroke. However, owing to the variation in the angle between the wing and the free-stream velocity, the relative velocity also changes such that it is a maximum at mid-downstroke and a minimum at mid-upstroke.

To test Dickson & Dickinson's (2004) idea on a typical flapping wing motion, we recalculated the lift and drag coefficients for our simulations using the instantaneous relative velocity. This was computed at the wing's radius of gyration ($r=0.57R$), so that the force coefficients returned the same values for $J=0$ as calculated previously. The variations in the instantaneous lift and drag coefficients are shown in figure 8, where the lift and drag coefficients are labelled as C_{Li} and C_{Di} , respectively, to denote the use of U_i . Note that here we approximated the relative velocity to be $U_i \approx r\Omega \pm V \cos \phi(t)$, where Ω is the rotational velocity of the wing at mid-stroke as defined in § 2.1. This was done to avoid excessive spikes in the coefficients around stroke reversal where the velocities are low. Figure 8 reveals that the instantaneous lift and drag coefficients are more comparable during the downstroke between advance ratios, but there is still some variation in coefficients outside of the stroke reversal times. This can be seen particularly in the instantaneous lift coefficient, which reduces by 18.6% between $t^* = 0.6$ and 0.9 for $J = 0.5$ but increases by 20.4 and 18.9% for $J = 0$ and 0.25 , respectively. Note that over this period ($0.6 \leq t^* \leq 0.9$) the wing is rotating at a constant rotational velocity and at a constant angle of attack, as in Dickson & Dickinson's (2004) experiment. For the upstroke the instantaneous lift and drag coefficients vary markedly with advance ratio. Thus, the use of the instantaneous velocity to collapse the force coefficients does not seem to apply for a normal flapping motion. This is likely to be due to the wing's acceleration and the re-establishment of the flow structures which are introduced by the flapping motion due to stroke reversal. These transient effects were purposely avoided in Dickson & Dickinson's (2004) rotating wing experiment. This highlights that the change in aerodynamic forces throughout a typical flapping cycle at non-zero advance ratios (figure 6) is not purely due to the relative velocity experienced by the wing, but also incorporates a change in flow structures that alter the wing's performance. The variations in vortex structures during the up- and downstrokes for non-zero advance ratios are investigated below.

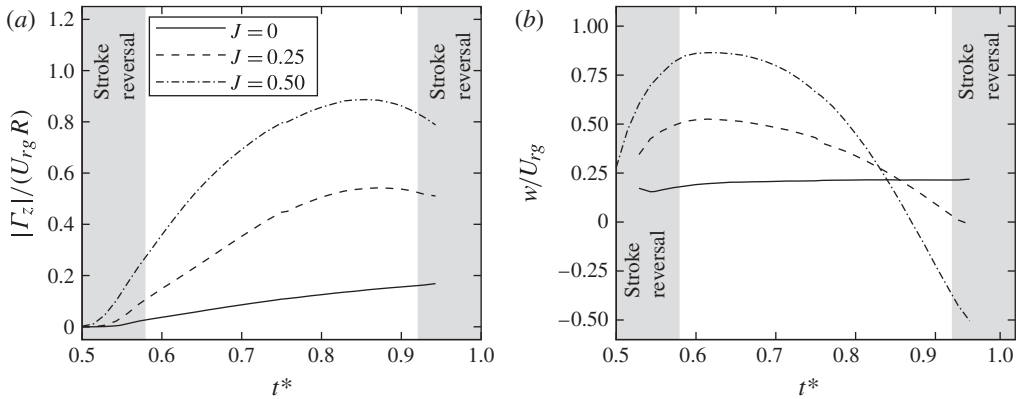


FIGURE 9. Time variation of (a) magnitude of LEV circulation ($|\Gamma_z|/U_{rg}R$) and (b) average spanwise velocity within the LEV (w/U_{rg}) at 25% span throughout the downstroke ($AR = 2.91$, $Re_R = 613$).

3.2.2. Downstroke flow structures

The added relative velocity seen by the wing during the downstroke at non-zero advance ratios causes an increase in the growth rate of circulation of the LEV. This can be seen in figure 9(a), which shows the time variation in circulation of the LEV at 25% span (for comparison with figure 21 later). This was calculated by integrating the vorticity within an area defined by a contour of the Q criterion. Figure 9(a) reveals a much more rapid increase in the LEV circulation for higher advance ratios, particularly in the early to mid-downstroke. Owing to the wing's rotation, a spanwise velocity is generated that acts from the wing's root to tip. This spanwise flow drains vorticity generated at the leading edge into the tip vortex (Ellington *et al.* 1996; Lentink & Dickinson 2009), and therefore the time evolution of circulation of the LEV is dependent on the balance between vorticity generation at the leading edge and vorticity transport due to the spanwise component of velocity. An increased rate of accumulation of circulation in the LEV is caused either by an increase in vorticity generation or by a reduction in vorticity transport. Figure 9(b) shows the average spanwise velocity within the vortex core, which demonstrates that during the early to mid-downstroke there is increased vorticity transport with advance ratio. Thus, the increase in circulation seen in figure 9(a) must be due to enhanced vorticity production at the leading edge as a result of the increased relative velocity experienced by the wing, and this increased production must outweigh the increased vorticity transport.

To investigate this further, the generation of vorticity near the wing's leading edge was assessed. Vorticity is generated at the boundary between the wing's surface and the fluid due to tangential pressure gradients and the tangential acceleration of the wing's surface (Morton 1984). The generated vorticity is then diffused into the fluid and advected around the leading edge, into the LEV. The method used to calculate the two production mechanisms is detailed in appendix A, and the results of this analysis are presented in figure 10, where the vorticity production is given as the temporal gradient of LEV circulation per unit span that is due to the generated vorticity. Figure 10(a) shows the influence that the tangential pressure gradient has on the production of vorticity at the leading edge throughout the downstroke at 25% span. During the period of constant-velocity rotation, the pressure gradient, and therefore

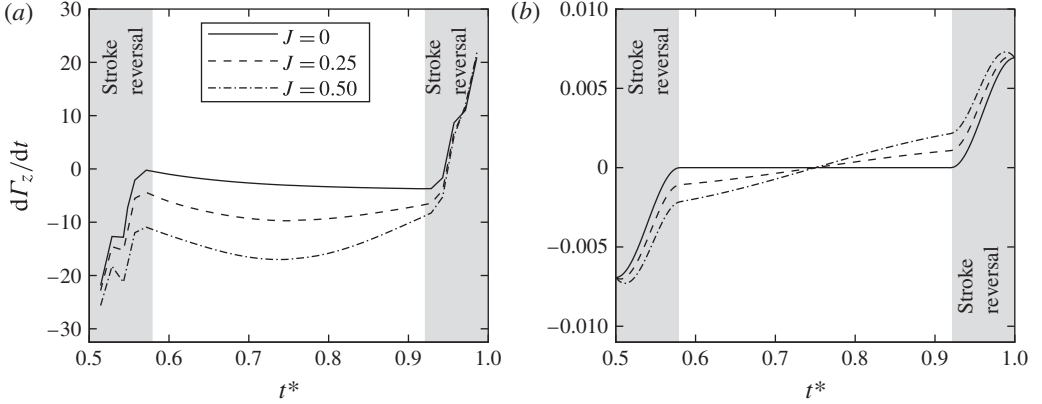


FIGURE 10. Change in vorticity generation throughout the downstroke for different advance ratios at 25% span. The vorticity generation is plotted as the time rate of change of circulation due to vorticity production per unit span ($d\Gamma_z/dt$). (a) The component due to the tangential pressure gradient on the wing’s surface. (b) The component due to the tangential acceleration of the wing’s surface. Appendix A details the calculation of these two quantities.

the generated vorticity, increases with increasing advance ratio. Furthermore, the production of vorticity follows a similar curve to the relative velocity, which leads to maximum vorticity production occurring around mid-downstroke for non-zero advance ratios. The vorticity generation due to the wing’s acceleration is plotted in figure 10(b). Here the wing’s acceleration produces negative vorticity for the first half of the downstroke and positive vorticity for the second half. However, the magnitude of the rate of generated circulation due to the wing’s acceleration is four orders of magnitude lower than that due to tangential pressure gradients. Hence, the pressure gradients around the wing’s leading edge dominate the generation of vorticity and the overall vorticity generation follows the curves shown in figure 10(a). This further demonstrates that increasing the advance ratio, and therefore the relative velocity, causes increased production of vorticity during the downstroke, which leads to an increased rate of accumulation of circulation in the LEV.

Owing to the low Reynolds number and therefore high viscous diffusion, the higher LEV circulation for non-zero advance ratios results in an increase in the size of the LEV. This can be seen in figure 11, which illustrates the change in spanwise vorticity at one instant during the downstroke ($t^* = 0.75$) for three advance ratios. Figure 11 shows that there is a larger region of negative vorticity with increasing advance ratio. This larger LEV structure is consistent with the higher LEV circulation shown in figure 9(a). Furthermore, the growth in the LEV’s size with advance ratio can also be seen in figure 12, which illustrates the three-dimensional change in vortex structures near the wing at three instances during the downstroke for three advance ratios. The left column is for a hovering ($J=0$) aspect-ratio 2.91 wing, and the middle and right columns are for advance ratios of 0.25 and 0.5, respectively, at the same aspect ratio. Figure 12 shows that, at each point in the downstroke, the higher the advance ratio, the larger the LEV. The tip and root vortices also enlarge with increasing advance ratio, and all the vortex structures continue to develop as the wing progresses through the downstroke. The increased growth rate of the LEV and TV leads to these vortices

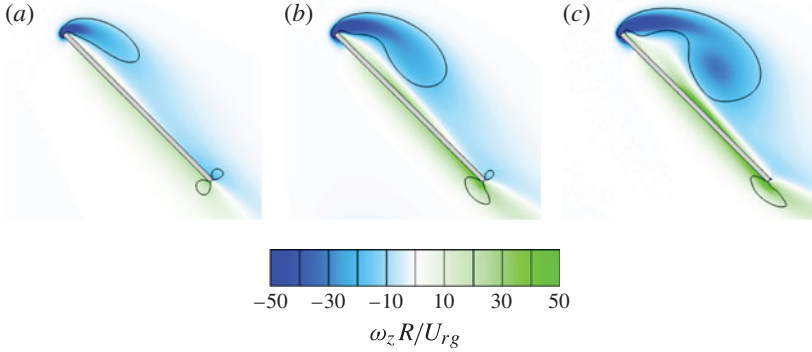


FIGURE 11. (Colour online) Spanwise vorticity contours at mid-downstroke ($t^* = 0.75$) at 50% span for three advance ratios ($AR = 2.91$, $Re_R = 613$): (a) $J = 0$, (b) $J = 0.25$ and (c) $J = 0.5$. The solid line is a single contour of the Q criterion that was used in figure 12.

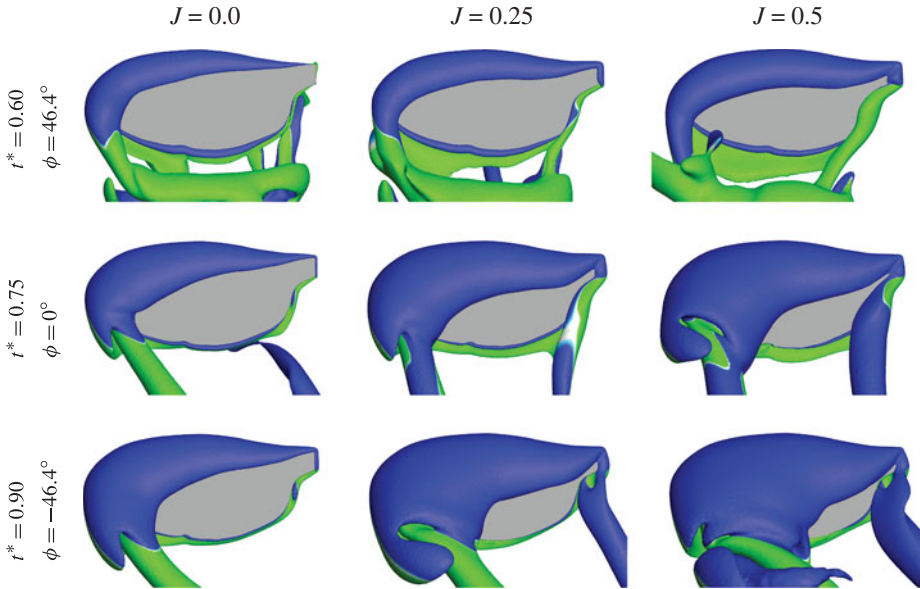


FIGURE 12. (Colour online) Flow structures during the downstroke for $J = 0$ (left), $J = 0.25$ (middle) and $J = 0.5$ (right). Images are taken perpendicular to the wing's top surface and are shown for early downstroke (top), mid-downstroke (middle) and late downstroke (bottom) ($AR = 2.91$, $Re_R = 613$). Vortex structures are visualised by iso- Q surfaces shaded (coloured online) by spanwise vorticity to indicate direction: mid grey (green online) is positive and dark grey (blue online) is negative. See also supplementary movies 1 and 2 for the $J = 0$ and $J = 0.5$ cases, respectively.

becoming so large for high advance ratios that they almost completely cover the entire wing in the latter stages of the downstroke (e.g. $t^* = 0.9$, $J = 0.5$).

When the LEV becomes too large, the flow no longer reattaches to the wing's top surface. This can be seen in the images in figure 13(a), which depict the change in two-dimensional streamlines throughout the downstroke at 50% span for the $J = 0.5$ case. Early in the downstroke, when the LEV is small, the flow separates from the

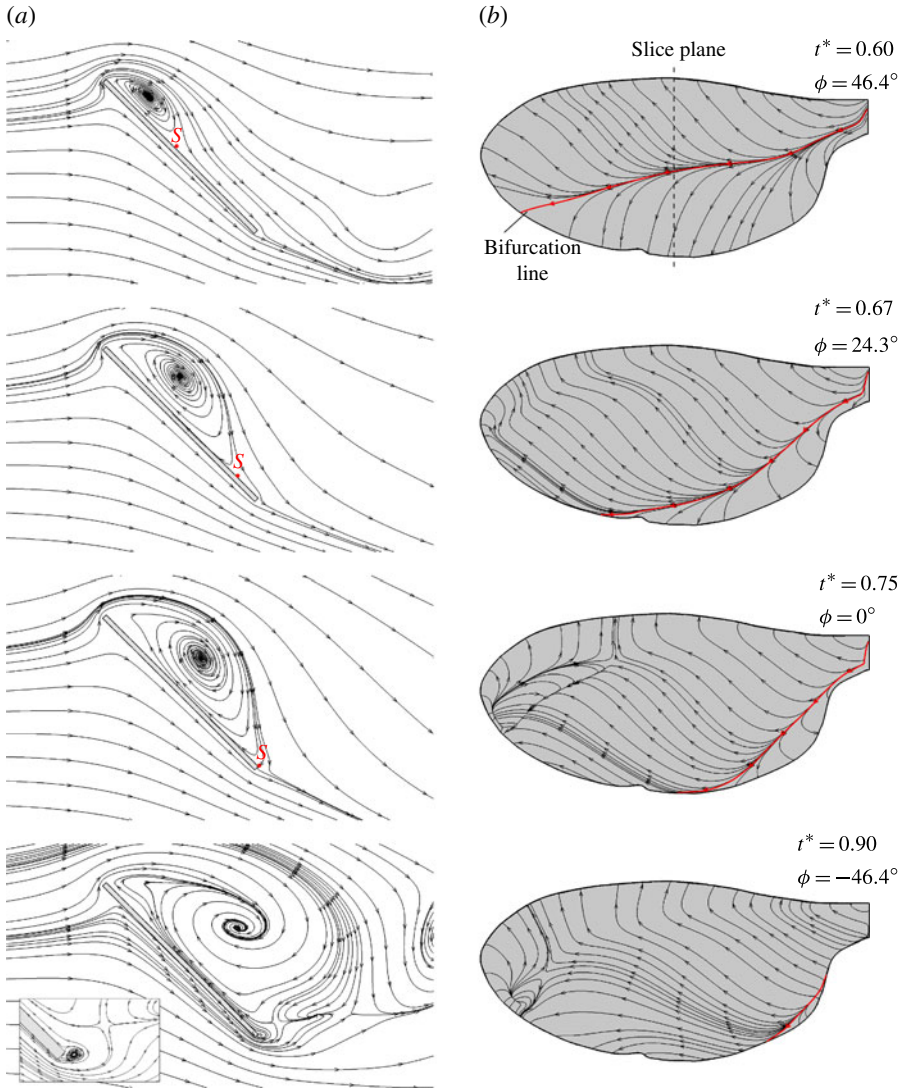


FIGURE 13. (Colour online) Flow topology images throughout the downstroke for the $AR = 2.91$ wing at $J = 0.5$ and $Re_R = 613$. (a) Two-dimensional streamlines at 50% span. 'S' marks the half saddle point on the wing's top surface and the inset in the bottom image displays a close-up of the flow topology at the wing's trailing edge. (b) Surface streamlines.

leading edge but reattaches to the wing just downstream of the LEV, as demonstrated by the half saddle point on the top surface of the wing. As the wing moves through the downstroke, the LEV enlarges and this pushes the reattachment point towards the trailing edge. Eventually the saddle point reaches the trailing edge ($t^* = 0.75$) and the flow no longer reattaches to the wing. This leads to a breakdown of the Kutta condition and the formation of a TEV ($t^* = 0.90$).

Figure 13(b) shows the surface streamlines on the wing's top surface. During the early part of the downstroke, a positive bifurcation line extends from the wing root to tip, which is associated with the reattachment of the flow downstream of the LEV.

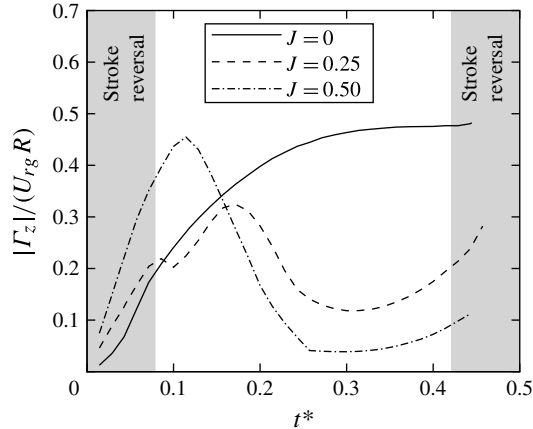


FIGURE 14. Time variation of the magnitude of total LEV circulation ($|\Gamma_z|/U_{fg}R$) at 60% span throughout the upstroke ($AR = 2.91$, $Re_R = 613$).

Because the LEV is conical in shape, as it grows in size the flow reattachment first reaches the trailing edge near the wing tip. As it continues to enlarge and the TV extends from the wing tip, the bifurcation line is shifted towards the trailing edge and the wing's root. This results in the bifurcation line reaching the trailing edge earlier along the wing's span, which indicates that the flow does not reattach to the wing over a larger proportion of the wing's span. By the end of the downstroke ($t^* = 0.9$), almost the entire wing experiences fully separated flow. The significance of this finding will be discussed further in §§ 3.4 and 3.5.

3.2.3. Upstroke flow structures

The variation in relative velocity for the upstroke is the opposite to the downstroke in that it decreases with increasing advance ratio. Figure 7 illustrates that for the upstroke ($0 \leq t^* \leq 0.5$) the velocity experienced by the wing is not only reduced for higher advance ratios, but also varies throughout the upstroke such that it is a maximum just before and after each stroke reversal, and it is a minimum at mid-upstroke. This therefore leads to both an overall reduction in vorticity generation at the leading edge with increasing advance ratio and a significant drop in vorticity production around mid-upstroke for non-zero advance ratios. The higher the advance ratio, the larger the variation in vorticity production throughout the upstroke.

This results in a significant variation in the circulation of the LEV throughout the upstroke for non-zero advance ratios. This is highlighted in figure 14, which shows the variation in LEV circulation at 60% span for three advance ratios. For the hovering case, the time variation in LEV circulation is the same as for the downstroke, although note that the circulation is higher in figure 14 than in figure 9, as the former is calculated further out along the wing's span. A 60% wing span was chosen for figure 14 for the upstroke, as the flow becomes locally reversed at high advance ratios at 25% span. Here the LEV's circulation increases during the early to mid-upstroke and then flattens out to become approximately constant towards the end of the stroke. Increasing the advance ratio results in an initial increase in the growth rate of circulation in the early part of the stroke due to the enhanced wake capture mechanism observed for the upstroke with increasing advance ratio (see figure 6). However, as the wing approaches mid-upstroke, the circulation in the LEV rapidly

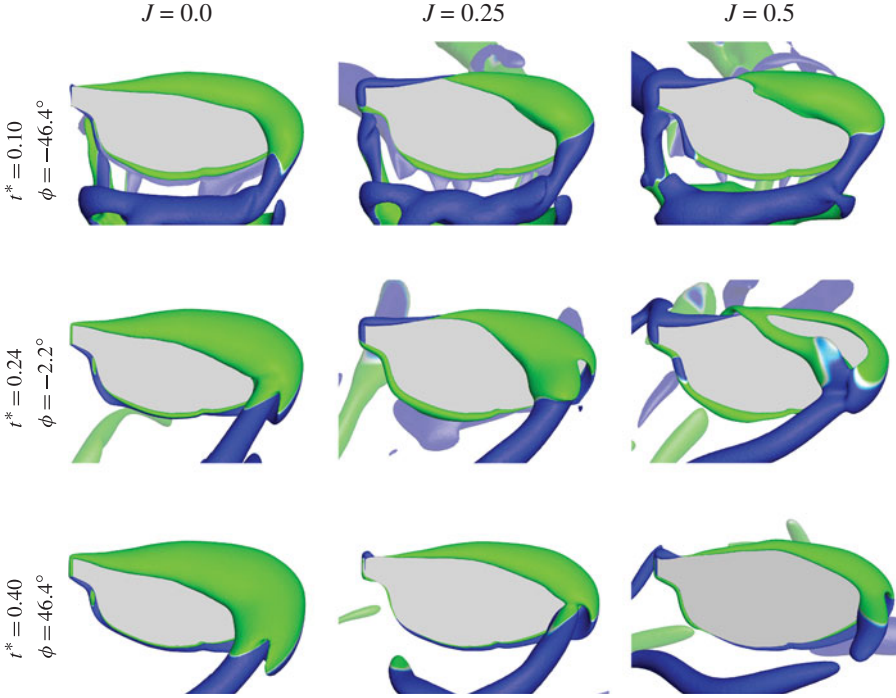


FIGURE 15. (Colour online) Flow structures during the upstroke for $J = 0$ (left), $J = 0.25$ (middle) and $J = 0.5$ (right). Images are taken perpendicular to the wing's surface and are shown for early upstroke (top), mid-upstroke (middle) and late upstroke (bottom) ($AR = 2.91$, $Re_R = 613$). Vortex structures are visualised by iso- Q surfaces shaded (coloured online) by spanwise vorticity to indicate direction: mid grey (green online) is positive and dark grey (blue online) is negative. Faded vortex structures are left over from the previous downstroke and are behind the wing.

drops as the vorticity production reduces. After mid-upstroke the LEV's circulation grows again as the relative velocity and vorticity generation increase.

The time variation in vorticity generation and LEV circulation causes a substantial change in the vortex structures around the wing during the upstroke for non-zero advance ratios. Figure 15 depicts the change in vortex structures near the wing at three instances during the upstroke for three advance ratios. The left column is for a hovering ($J = 0$) aspect-ratio 2.91 wing, which demonstrates that the upstroke flow structures are identical to the downstroke except with opposite sign of rotation. The middle and right columns are for advance ratios of 0.25 and 0.5, respectively. As the free-stream velocity is acting with the wing's rotation, a region of reversed flow is created near the wing's root, and thus the LEV is restricted to being in the outer part of the wing for non-zero advance ratios. In the early upstroke ($t^* = 0.1$), the LEV is larger due to the enhanced wake capture mechanism. However, by middle to late upstroke the LEV is smaller for larger advance ratios. Increasing the advance ratio also allows the tip vortex and wake structures to remain close to the wing.

At an advance ratio of 0.5, the iso- Q surface representing the LEV can be seen to split, revealing a dual LEV structure. This dual vortex structure was only observed at this advance ratio and must be due to the very low relative velocity around mid-upstroke at this advance ratio. Around mid-upstroke, the low relative velocity causes

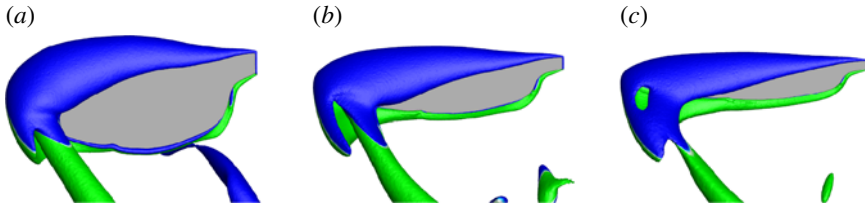


FIGURE 16. (Colour online) Vortex structures at mid-downstroke ($t^* = 0.75$) for three aspect-ratio wings ($J = 0$, $Re_R = 613$): (a) $AR = 2.91$, (b) $AR = 5.10$ and (c) $AR = 7.28$. Images are taken perpendicular to the wing's top surface and vortex structures are visualised by iso- Q surfaces shaded (coloured online) by spanwise vorticity to indicate direction: mid grey (green online) is positive and dark grey (blue online) is negative.

both low vorticity generation and a low advection velocity. This allows the LEV that is created from wake capture earlier in the stroke to break away from the leading edge. A new LEV is created behind it, resulting in the dual vortex structure. As the downstream LEV is no longer fed vorticity from the leading edge, it quickly cross-annihilates with a region of opposite-sign vorticity on the wing's surface and possibly with the tip vortex due to its close proximity. Hence by the late upstroke ($t^* = 0.4$) the downstream LEV has gone, leaving only the smaller LEV near the leading edge. This variation in flow structures throughout the upstroke explains the significant change in instantaneous force coefficients observed in figure 8.

3.3. Effect of aspect ratio

Here we consider the effect of aspect ratio at an advance ratio of zero; however, the effect of aspect ratio applies equally to other flight speeds. Figure 16 shows the vortex structures near the wing at mid-downstroke for three different aspect-ratio wings. As was found in an earlier study (Harbig *et al.* 2013) and can also be seen here, by scaling the flow using a span-based Reynolds number, a very similar vortex structure is created over each of the different aspect-ratio wings. Figure 16 demonstrates that the size of the LEV is approximately constant relative to the wing's span between each aspect-ratio wing. Thus, modifying the wing's aspect ratio can be seen as effectively changing the wing's chord length relative to a fixed LEV size. This leads to the LEV being much larger in proportion to the wing for higher aspect ratios.

It does not matter how the wing's aspect ratio is changed (by stretching the wing in either the chordwise or spanwise directions), this condition is still met if the flow is scaled using the span-based Reynolds number. If the span-based Reynolds number is not maintained, and either the conventional chord-based Reynolds number is used or no scaling is made, then increasing the aspect ratio still leads to a larger LEV relative to the wing's size but it also includes a change in the structure of the LEV due to an alteration of the span-based Reynolds number (Harbig *et al.* 2013).

3.4. Leading-edge vortex stability

In this section, we first consider a case in which the effects of advance ratio and aspect ratio are combined. We found that at high aspect ratios and high advance ratios the LEV becomes unstable and is shed from the wing during the downstroke. An example of this can be seen in figure 17, which shows the change in spanwise vorticity during the early stages of the downstroke at 70% span for an $AR = 7.28$ wing

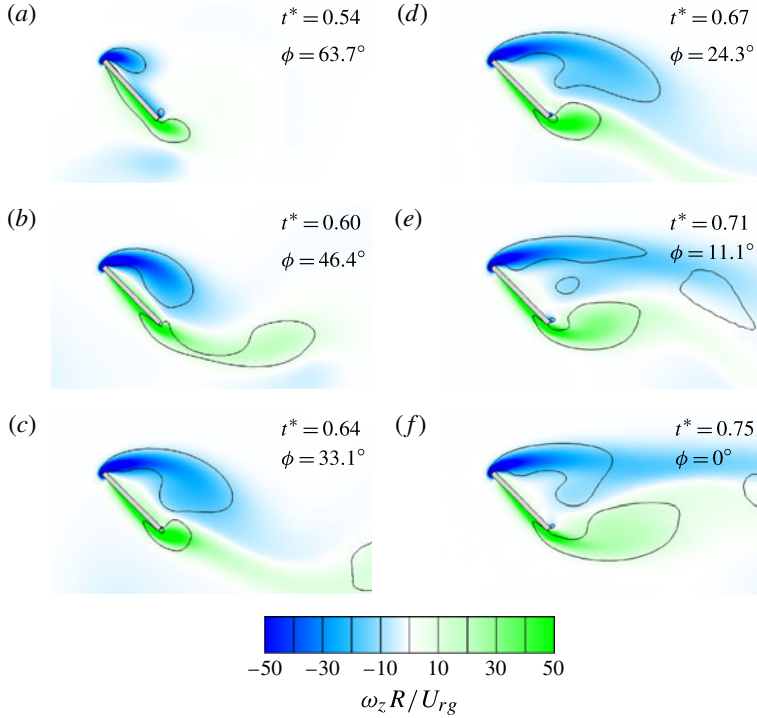


FIGURE 17. (Colour online) Spanwise vorticity contours at 70 % span for $AR=7.28$ wing at $J = 0.5$ and $Re_R = 613$. The solid line is a single contour of the Q criterion. The sequence progresses from (a) to (f).

at $J = 0.5$. The black lines are a single contour of the Q criterion. At the beginning of the downstroke ($t^* = 0.54$) the LEV and TEV form. The TEV is soon shed from the wing and the LEV quickly grows to become as large as the wing's chord length. At this point ($t^* = 0.64$) the flow can no longer reattach to the wing's top surface. The Kutta condition breaks down and vorticity forms at the trailing edge. As the wing continues through the downstroke, the LEV is eventually shed into the wake ($t^* = 0.71$) and the TEV grows in size.

This process is remarkably similar to the initial flow patterns created by a translating wing, as described by Dickinson & Gotz (1993) from their two-dimensional wing towing tank experiments. However, figure 18 (see also supplementary movie 3) shows a three-dimensional view of this shedding process, which illustrates that it is not two-dimensional. Figure 18 reveals that the LEV and TEV form part of a vortex loop that is shed from the wing. In the early stages of the downstroke ($t^* = 0.6$) the TEV_1 is shed from the wing and the LEV_1 quickly grows to envelop the entire wing. The LEV_1 and TEV_1 are connected by the TV to form a ring vortex that extends back to the wing's root. As the wing continues to rotate, the LEV_1 peels away from the outer part of the wing and a new TEV_2 begins to form. By mid-stroke ($t^* = 0.75$) LEV_1 has completely shed from the outer 50% of the wing. For this aspect-ratio wing, at this advance ratio, the shedding of the LEV seems to be confined to the outer half of the wing. A new LEV_2 has begun to form in its place and the second TEV_2 has separated from the wing near the wing tip. The shed LEV_1 and TEV_1 form a counter-rotating vortex pair in the wake of the wing and are part of a vortex loop

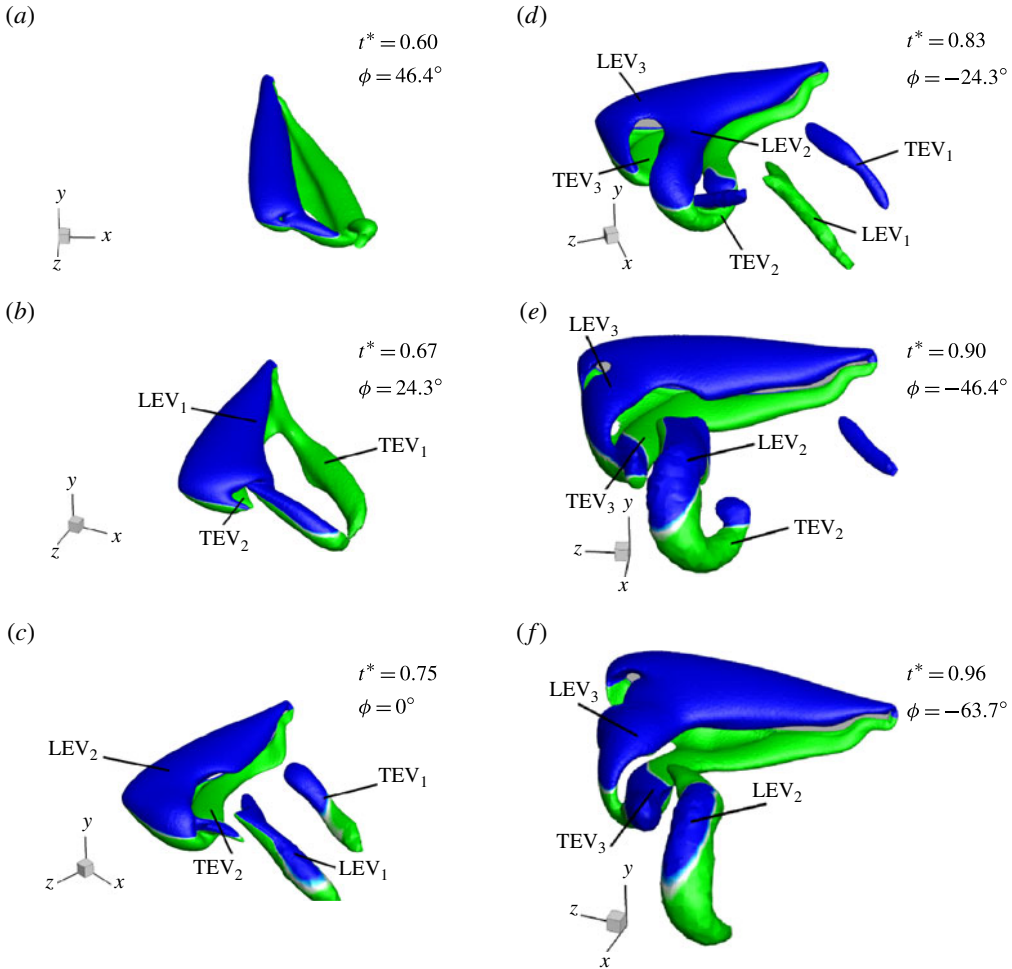


FIGURE 18. (Colour online) Stationary view of the wing’s motion (clockwise rotation) and the generated flow structures during the downstroke for an $AR=7.28$ wing at $J=0.5$ and $Re_R=613$. Vortex structures are visualised by iso- Q surfaces shaded (coloured online) by spanwise vorticity to indicate direction: mid grey (green online) is positive and dark grey (blue online) is negative. The sequence progresses from (a) to (f). See also supplementary movie 3.

that remains connected to the wing. Note that the change in grey scale (colour) of LEV_1 and TEV_1 in figure 18 at $t^*=0.83$ is due to their change in orientation relative to the wing and not due to a change in sign.

For this particular case, this shedding process is repeated two more times before the end of the downstroke, where LEV_2 and TEV_2 are shed from the wing tip as part of a vortex loop that peels away from the wing tip with the TEV leading the detachment. A third vortex loop is formed, consisting of LEV_3 and TEV_3 , and it is also shed before the end of the wing’s motion.

It was found that under hovering conditions ($J=0$) the LEV remains attached to the wing for a variety of aspect ratios. However, at high advance ratios the LEV is stable for low-aspect-ratio wings (figure 12) but is unstable for large-aspect-ratio wings

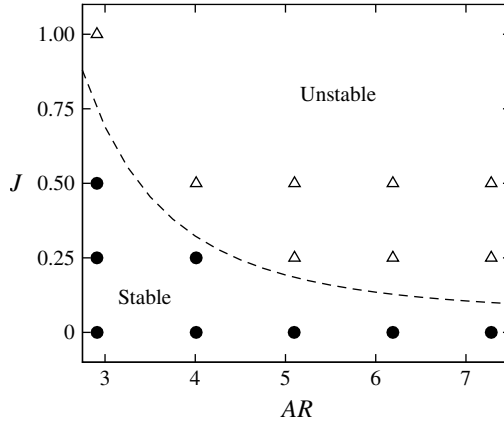


FIGURE 19. Stability of the LEV for a range of AR and J at $Re_R = 613$. Symbols denote cases where LEV shedding is (Δ) and is not (\bullet) observed during the downstroke. The dashed line represents the approximate boundary between the two states.

(figure 18). Therefore, the stability of the LEV is dependent upon both the advance ratio and the wing's aspect ratio. This relationship is shown in figure 19, which maps the stability of the LEV from our simulations. It can be seen that, for a particular aspect ratio, if the advance ratio is increased, the LEV can become unstable. Likewise, for a constant advance ratio, if the wing aspect ratio is increased to be large enough, the LEV can become unstable.

For a two-dimensional translating wing, the LEV becomes unstable once it grows too large for the wing, such that the flow can no longer reattach to the wing's top surface (Dickinson & Gotz 1993). When this occurs, the Kutta condition breaks down and a trailing-edge vortex forms. If the wing continues its motion, the LEV is eventually shed and the wing is said to have stalled. The stability of the LEV is therefore related to the size of the LEV relative to the wing's chord length. Figures 17 and 18 depict this same shedding process for our simulations but it is now modified to be three-dimensional due to the wing's rotation and finite span.

In § 3.2.2 we revealed that increasing the advance ratio increased the growth rate of the LEV, and in § 3.3 we showed that increasing the wing aspect ratio effectively shortens the wing's chord. Both of these parameters has the same end effect of creating a LEV that is a larger proportion of the wing's chord length. Therefore, combining these two mechanisms together can cause situations in which the LEV becomes too large for the wing. The higher the advance ratio or aspect ratio, the earlier in the downstroke that the LEV becomes as large as the wing's chord length, and thus the LEV can be shed if there is sufficient rotation left in the downstroke. In figure 19, the points below the line represent cases where the LEV is either smaller than the wing's chord length or just reaches a comparable size late in the downstroke. Points above the line constitute instances when the LEV becomes as large as the wing's chord earlier in the downstroke and thus the LEV is shed before the end of the downstroke. The further above and to the right of the line, the more unstable the LEV is, which can lead to it being shed multiple times.

Thus, the stability of the LEV is dependent on the growth rate of the LEV (determined by J) and the relative size of the LEV compared to the wing's chord length (determined by AR).

3.5. Aerodynamic performance

In this section, the effect of LEV stability on the wing's aerodynamic performance is discussed. Dickinson & Gotz (1993) reported that, for their two-dimensional translating wing, the lift force decreased as the Kutta condition broke down and a TEV formed, as the wing became less effective at imparting a steady downward momentum to the fluid (Sane 2003). After the LEV was shed from the wing, the time-averaged lift had reached a minimum and the wing was said to have stalled. This observation from a two-dimensional flow can be applied to our flapping wing simulations to explain the variation in wing performance.

In § 3.2.1 it was shown that the instantaneous lift coefficient decreased throughout the downstroke at an advance ratio of 0.5, but increased for lower advance ratios (figure 8). In § 3.2.2 it was found that, for this high-advance-ratio case, a larger proportion of the wing developed fully separated flow as the LEV grew and the wing moved through the downstroke (figure 13). Thus the gradual reduction in instantaneous lift coefficient throughout the downstroke is due to the wing becoming less effective at producing lift in the region of the wing that experiences fully separated flow. As this region enlarges, the wing's overall performance drops. At lower advance ratios the LEV growth is slower and hence less of the wing experiences fully separated flow and a loss in performance.

This idea can be extended further to understand the effect of aspect ratio on the wing's performance. Figure 20(a,b) shows the variation in average lift and drag coefficients, respectively, with aspect ratio for three advance ratios. The white open symbols are the average values during the downstroke, the black filled symbols are for the upstroke and the grey filled symbols are the average values over the whole flapping cycle. Figure 20(a,b) demonstrates that the force coefficients are increased with increasing advance ratio for the downstroke but are reduced for the upstroke due to the change in relative velocity. At a particular advance ratio, the aerodynamic forces are roughly constant for the upstroke over a range of aspect ratios. However, for the downstroke the aerodynamic forces reduce with increasing aspect ratio. This variation in aerodynamic forces can be explained by the development of separated flow across the wing. Figure 13 illustrates that, for the $AR = 2.91$ wing at $J = 0.5$, almost the entire wing experiences fully separated flow late in the downstroke. As explained in § 3.3, increasing the wing aspect ratio effectively shortens the wing's chord length and thus this state is reached earlier in the downstroke for higher aspect ratios. Therefore, higher aspect ratios have lower aerodynamic performance over a greater proportion of the downstroke. Furthermore, in § 3.4 it was shown that higher aspect ratios can shed the LEV from the outer part of the wing and this further reduces lift. Consequently, higher-aspect-ratio wings have lower average aerodynamic forces over the downstroke. This effect is more pronounced for higher advance ratios due to the increased growth rate of the LEV.

The lower aerodynamic forces associated with higher aspect ratios leads to these wings having reduced aerodynamic performance during the downstroke. As the downstroke dominates the force balance at non-zero advance ratios, this leads to a reduction in the overall wing performance for higher aspect ratios. This can be seen in figure 20(c,d), which plots the full cycle average values of the lift on drag ratio (C_L/C_D) and power factor ($C_L^{3/2}/C_D$), respectively, over a range of aspect ratios. The power factor is inversely proportional to the power required to generate a certain amount of lift (Wang 2008) and therefore maximising it maximises aerodynamic performance. Figure 20(d) shows that aspect ratios of 3–4 have increased power

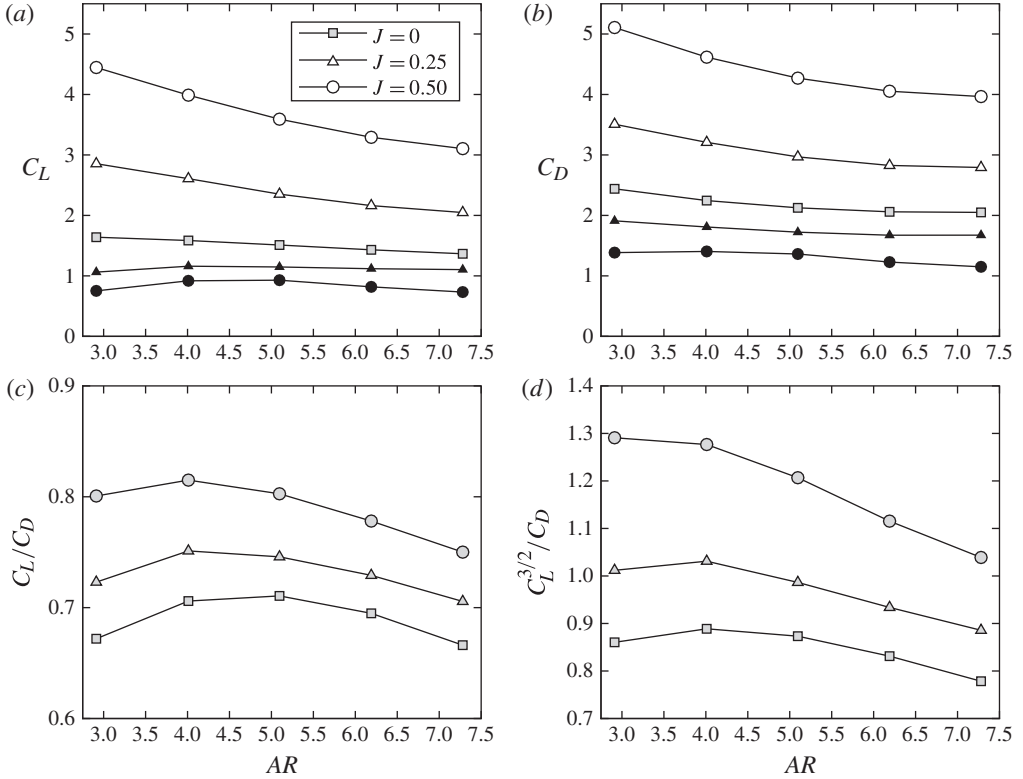


FIGURE 20. Aerodynamic force graphs ($Re_R = 613$); average (a) lift coefficient, (b) drag coefficient, (c) lift on drag ratio and (d) power factor. White open symbols are average values for the downstroke, black filled symbols are for the upstroke and grey filled symbols are the average values over the full flapping cycle.

factors compared to higher aspect ratios. This highlights that lower-aspect-ratio wings out-perform high aspect ratios under insect-like flight regimes, as they are able to maintain a smaller attached LEV over a wider range of advance ratios.

4. Results at high Reynolds number

It is well known that the characteristics of the LEV change with Reynolds number. As the Reynolds number is increased, the LEV forms a much tighter spiral structure compared to at low Reynolds numbers, and a strong axial velocity develops in its core (Birch *et al.* 2004; Liu & Aono 2009). The LEV is often observed to break down at some point along the wing's span (Lu, Shen & Lai 2006; Lentink & Dickinson 2009; Venkata & Jones 2013). A second co-rotating LEV structure has also been reported to form as the primary LEV develops with Reynolds number (Lu *et al.* 2006). This vortex forms between the leading edge and the primary LEV, which results in a dual LEV structure. All of these changes in flow structure are observed in our simulations as the Reynolds number is increased from 613 to 7668, including the formation of the dual LEV structure. For more detailed information on the change in flow structure with Reynolds number seen in our simulations, see Harbig *et al.* (2013). In this section the effects of advance ratio and aspect ratio are investigated at the higher Reynolds number of 7668.

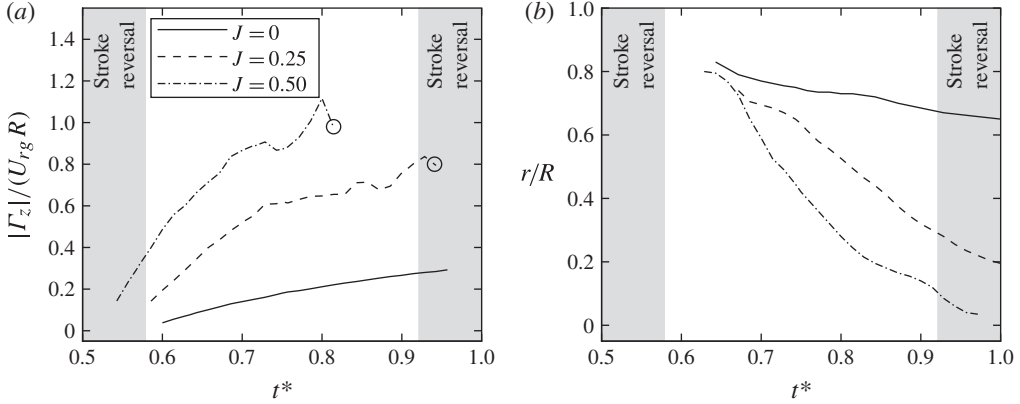


FIGURE 21. LEV graphs at $Re_R = 7668$ for the $AR = 2.91$ wing. (a) Time variation of the magnitude of total LEV circulation ($|\Gamma_z|/U_{rg}R$) at 25% span throughout the downstroke. Open circles show the point in the downstroke at which the breakdown point of the LEV reaches 25% span. Note that 25% span was chosen for this graph in order to avoid LEV breakdown as much as possible. (b) Variation in the spanwise location of LEV breakdown (r/R) throughout the downstroke.

4.1. Effect of advance ratio

The effect of advance ratio at the higher Reynolds number is essentially the same as at the lower Reynolds number. The added free-stream velocity reduces the relative velocity experienced by the wing for the upstroke and increases it for the downstroke. The increased relative velocity for the downstroke enhances vorticity production, which leads to an increased growth rate of LEV circulation with increasing advance ratio. This can be seen in figure 21(a), which shows the LEV circulation at 25% span throughout the downstroke for three advance ratios.

At this Reynolds number, however, the increased circulation of the LEV does not result in a larger LEV structure due to viscous diffusion, as the effect of viscosity is markedly reduced due to the higher Reynolds number. Instead, the increased circulation leads to an earlier breakdown of the primary LEV. Vortex breakdown is an abrupt change in the structure of a vortex with a marked retardation of the flow in the axial direction (Hall 1972). When a vortex breaks down, the vortex core expands downstream of the breakdown point and the flow within it becomes turbulent (Leibovich 1978). This can be seen in figure 22, which shows the change in the vortex structures at three instants during the downstroke for $J = 0, 0.25$ and 0.5 . At each point in the downstroke (e.g. $t^* = 0.75$), the spanwise position of the breakdown location of the LEV moves towards the wing root with increasing advance ratio. When the LEV breaks down, the vortex core rapidly expands in size and a region of unsteady flow is generated across the rest of the wing's span. Thus the growth of the LEV appears to be through vortex breakdown at this Reynolds number, rather than viscous diffusion.

Breakdown is observed to occur once a critical swirl ratio or swirl angle is reached, which is calculated from the ratio of the azimuthal velocity to the axial velocity in the vortex (Hall 1972). As the size of the LEV upstream of the breakdown point does not change significantly with advance ratio at this Reynolds number, the increased circulation results in an increase in the azimuthal velocity in the vortex core. This increases the swirl ratio and leads to the LEV breaking down closer to the wing's

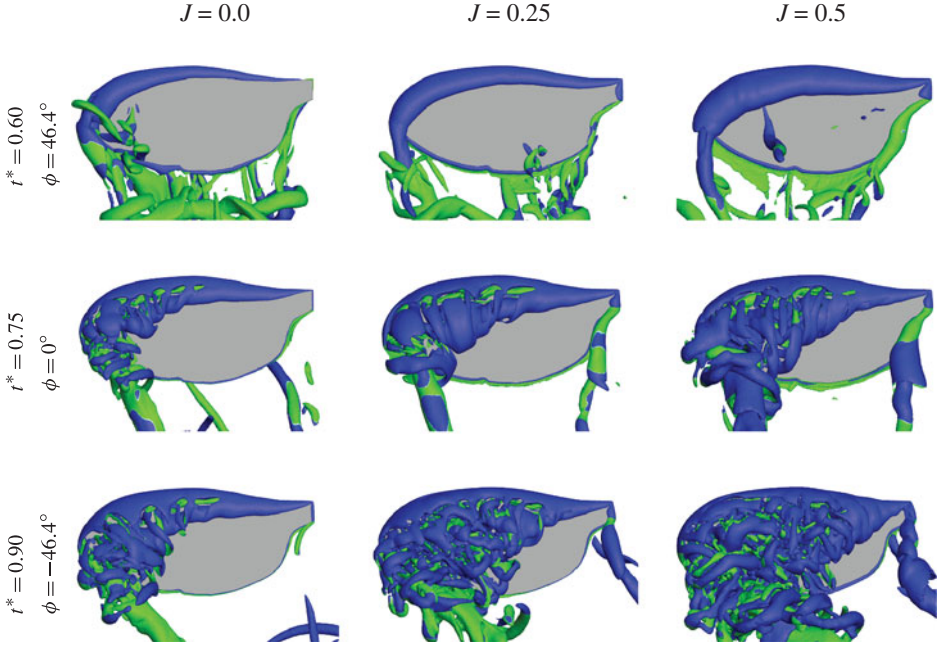


FIGURE 22. (Colour online) Flow structures during the downstroke for $J = 0$ (left), $J = 0.25$ (middle) and $J = 0.5$ (right). Images are taken perpendicular to the wing's top surface and are shown for early downstroke (top), mid-downstroke (middle) and late downstroke (bottom) ($AR = 2.91$, $Re_R = 7668$). Vortex structures are visualised by iso- Q surfaces shaded (coloured online) by spanwise vorticity to indicate direction: mid grey (green online) is positive and dark grey (blue online) is negative. See also supplementary movies 4 and 5 for the $J = 0$ and $J = 0.5$ cases, respectively.

root. Thus, the increased growth rate of circulation for non-zero advance ratios during the downstroke results in the breakdown location moving from the wing tip to the wing root more rapidly for higher advance ratios. This is shown in figure 21(b) and can also be seen in figure 22. Under hovering conditions, the LEV begins to break down near the wing tip at approximately $t^* = 0.64$. The breakdown location slowly moves towards the wing's root as the LEV circulation builds, and by the end of the downstroke the spanwise breakdown position is approximately 65% wing span. Increasing the advance ratio increases the rate at which the breakdown point moves towards the wing's root, and as such the breakdown location is closer to the wing's root by the end of the downstroke for higher advance ratios. At an advance ratio of 0.5, late in the downstroke the breakdown location is very close to the wing's root, and therefore a coherent LEV structure can no longer be seen on the wing, as all of the flow within the vortex has become unsteady (figure 22, $t^* = 0.9$, $J = 0.5$). The burst LEV structure once again can be seen to cover almost all of the wing at this point in the downstroke for high advance ratios. Hence, the increased circulation associated with higher advance ratios does still lead to an expansion of the LEV, but it is through vortex breakdown.

4.2. Effect of aspect ratio

The effect of wing aspect ratio at the higher span-based Reynolds number is the same as at the lower Reynolds number, where increasing the aspect ratio shortens the

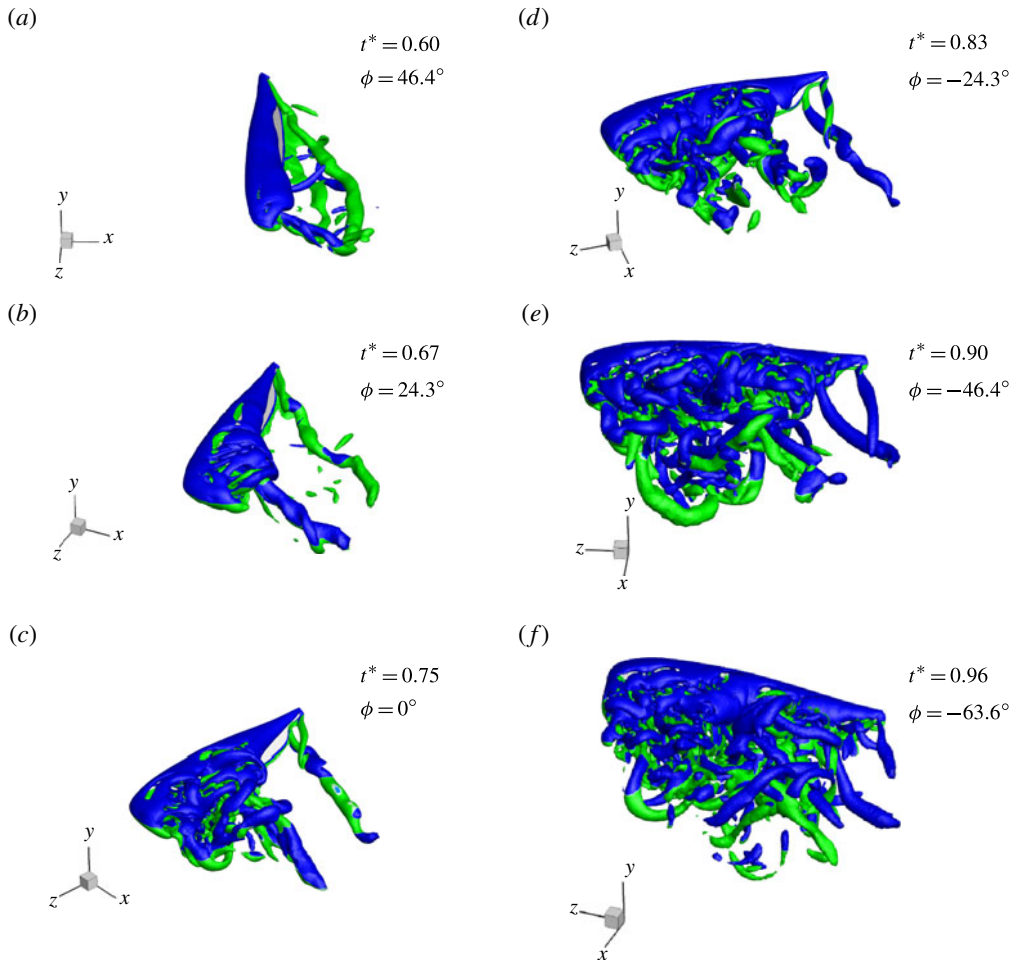


FIGURE 23. (Colour online) Stationary view of the wing's motion (clockwise rotation) and the generated flow structures during the downstroke for an $AR = 7.28$ wing at $J = 0.5$ and $Re_R = 7668$. Vortex structures are visualised by iso- Q surfaces shaded (coloured online) by spanwise vorticity to indicate direction: mid grey (green online) is positive and dark grey (blue online) is negative. The sequence progresses from (a) to (f). See also supplementary movie 6.

wing's chord length relative to the LEV's size. When the LEV breaks down, the vortex rapidly grows in size, and therefore combining this with a larger aspect ratio can result in vortex shedding. This can be seen in figure 23, which shows the vortex structures during the downstroke for the high-aspect-ratio ($AR = 7.28$) high-advance-ratio ($J = 0.5$) case at $Re_R = 7668$ (see also supplementary movie 6). At the beginning of the downstroke ($t^* = 0.6$), the vortex loop consisting of the LEV, TV and TEV can be seen. As the wing moves through the downstroke, the LEV breaks down, initially near the wing tip, but it rapidly moves towards the wing's root from then on. As it does so, the TV also moves in towards the root. This creates a very similar counter-rotating vortex pair in the wake of the wing ($t^* = 0.75$) as was seen at the lower Reynolds number (see figure 18), which suggests that the LEV is again shed from the outer part

of the wing for this case. Beyond the breakdown point, the flow is highly unsteady and, instead of large coherent vortex loops being shed from the wing, many smaller vortex structures are shed from both the leading and trailing edges. Towards the end of the downstroke, the LEV has completely burst, resulting in a flow that resembles highly unsteady separated flow. Hence, the LEV appears to be shed from the wing for this case.

In addition, at this advance ratio but for the lower-aspect-ratio wing, the LEV is not shed (see right-hand column of figure 22). Instead, the burst LEV structure closely resembles the LEV from the same case at the lower Reynolds number (figure 12).

Therefore, the stability of the LEV is again dependent on both the wing's aspect ratio and advance ratio in the same way as described in § 3.4, except that at this higher Reynolds number when shedding does occur it is not observed as a coherent structure due to the breakdown of the LEV and the unsteady flow that this creates.

5. Discussion

As highlighted in the Introduction, a number of different theories have been proposed as to how the stability of the LEV is maintained on insect wings. These include spanwise vorticity transport due to the spanwise component of velocity (Maxworthy 1979; Ellington *et al.* 1996; van den Berg & Ellington 1997), vortex tilting due to the downwash velocity (Birch & Dickinson 2001; Cheng *et al.* 2013) and rotational accelerations due to the low-Rossby-number rotation of the wing (Lentink & Dickinson 2009). These hypotheses generally attempt to explain the mechanism through which the growth of the LEV is controlled. In this paper, we did not directly test any of these theories, but we have shown that the LEV becomes unstable and is shed from the wing under certain conditions that are dictated by the advance ratio and wing's aspect ratio. The advance ratio controls the growth rate of the LEV during the downstroke, while the aspect ratio defines the maximum size that the LEV can become before flow separation occurs and the Kutta condition breaks down.

As LEV stability is partly determined by the advance ratio, which is a measure of the wing's rotation relative to its translation, a comment on the conformity of our results with the low-Rossby-number hypothesis of Lentink & Dickinson (2009) can be made. In an earlier study (Harbig *et al.* 2013), it was demonstrated that, when the span-based scaling is used, the Rossby number is equal to $Ro = U_{tip}/\Omega R$. Letting $U_{tip} = \Omega R \pm V$, where the velocities are summed for the downstroke and subtracted for the upstroke, results in $Ro = 1 \pm V/\Omega R \approx 1 \pm J$. Thus, the Rossby number is dependent on the advance ratio. It is equal to one for hovering flight, but is increased during the downstroke and reduced during the upstroke for non-zero advance ratios. Applying the low-Rossby-number hypothesis of Lentink & Dickinson (2009) predicts that the LEV would be unstable during the downstroke at high advance ratios. This prediction matches our findings, and therefore our results support the low-Rossby-number theory, at least in a general sense. However, the details of this theory have not been tested. The wing's rotation generates rotational accelerations and a spanwise pressure gradient that together produce the spanwise velocity, which is one candidate for LEV stability. However, whether the Coriolis acceleration itself directly provides stability for the LEV, as proposed by Lentink & Dickinson (2009), has not been confirmed.

Regardless of the mechanism through which the growth of the LEV is controlled, the shedding of the LEV is clearly a modification of the same delayed stall process

seen on a two-dimensional translating wing (Dickinson & Gotz 1993). We have demonstrated that the time it takes for the LEV to reach the critical size of one chord length depends on both the advance ratio and the wing's aspect ratio. If this time scale is shorter than the half-stroke period, then the LEV can be shed. Therefore, it can also be ascertained that the LEV stability would be dependent on the wing's stroke amplitude, as this determines the absolute size that the LEV can reach by the end of the downstroke. While different stroke amplitudes have not been tested here, changing the amplitude while maintaining a constant rotational velocity can be viewed as altering the half-stroke period (i.e. the flapping frequency must also change). Smaller amplitudes would therefore limit the vortex size and thus allow the LEV to remain attached to the wing for higher advance ratios and for larger aspect ratios. The idea that the LEV stability is dependent on the relative time scales of the delayed stall mechanism compared to the flapping motion has been proposed previously (Wang 2005), based on two-dimensional flapping wing simulations. Furthermore, as the wing's performance is affected by the LEV's stability, smaller stroke amplitudes may improve the aerodynamic performance of larger-aspect-ratio wings.

Finally, a comment needs to be made on the assumption of a constant stroke plane angle with flight speed that was made in the set-up of these simulations. As explained in §2.1, this assumption was made in order to simplify the analysis by taking out some of the complexity associated with including a variation in stroke plane angle with advance ratio. However, insects tilt their stroke plane significantly in order to achieve forward flight. In our simulations the stroke plane angle was set to 0° , which has also been used by Dickson & Dickinson (2004). Other studies have investigated the effect of advance ratio at different stroke plane angles. Nagai *et al.* (2009) studied a flapping bumblebee wing ($AR \approx 3$) for advance ratios of $0 \leq J \leq 0.47$ at a stroke plane angle of 45° . They observed a large but stable LEV formed during the downstroke. Gopalakrishnan & Tafti (2010) computed the flow around a flapping $AR = 4$ plate at $J = 0.5$ where the free-stream flow was perpendicular to the wing's stroke plane. They reported that the LEV was shed from the outer part of the wing mid-way through the downstroke. Bross *et al.* (2013) also investigated the effect of advance ratio at a stroke plane angle of 90° . They used PIV to measure the flow around a rotating $AR = 2$ plate. They found that the LEV was stable for all advance ratios tested ($0 \leq J \leq 0.537$), but they also observed that the streamline patterns departed from an attached flow state for large values of advance ratio and rotation angles. Combining all these observations together, we conclude that the effects of advance ratio and wing aspect ratio in determining the stability of the LEV are likely to apply to other stroke plane angles, and thus also to the flight of real insects. However, further investigation is warranted, especially considering the additional complexity that a varying non-zero stroke plane angle adds to the problem.

6. Conclusion

In this paper we have investigated the change in the LEV characteristics throughout a simulated flapping cycle over a range of aspect ratios and advance ratios using a numerical model of a flapping fruit-fly wing. Owing to the symmetric flapping kinematics between the up- and downstrokes, under hovering flight the vortex structures that are created for each half-stroke are identical, except with opposite signs of rotation. However, at non-zero advance ratios the change in relative velocity experienced by the wing for each half-stroke leads to very different vortex structures being created between the up- and downstrokes.

It was demonstrated that the relative velocity affected vorticity production on the wing. For the upstroke the relative velocity was reduced with increasing advance ratio, which resulted in less vorticity generation, particularly around mid-upstroke. This created smaller and weaker LEV structures for the upstroke at high advance ratios, that were confined to the outer portion of the wing owing to a region of reversed flow at the wing's root. For the downstroke, the relative velocity was increased with increasing advance ratio, which caused enhanced vorticity production. At low span-based Reynolds numbers, this resulted in a larger and stronger LEV being formed at higher advance ratios, where the LEV rapidly grew in size throughout the downstroke.

It was found that changing the wing aspect ratio had the effect of shortening the wing's chord length relative to the LEV's size. When the effects of wing aspect ratio and advance ratio were combined, the LEV quickly grew to envelop the entire wing during the downstroke and eventually it was shed as part of a vortex loop that peeled away from the wing's tip. Thus, the stability of the LEV is dependent on both the advance ratio and wing aspect ratio, which control the growth rate of the LEV and the relative size of the LEV compared to the wing's chord length, respectively. The higher the aspect ratio or advance ratio, the more unstable the LEV becomes. This helps to explain why many insects have evolved to have low-aspect-ratio wings, as low aspect ratios avoid LEV shedding over a wider range of advance ratios.

Indeed, it was shown that the mean downstroke lift coefficient reduces as the wing aspect ratio is increased. This was due to the wing stalling, and therefore becoming less effective at producing lift, when the LEV became too large and was shed from the wing. Low-aspect-ratio wings therefore outperformed higher aspect ratios, particularly at non-zero advance ratios. Hence, MAV designers who wish to employ an insect-like flapping wing mechanism should use low-aspect-ratio wings for optimal aerodynamic efficiency over a wide range of flight speeds.

At higher span-based Reynolds numbers, the primary LEV was observed to break down at some point along the wing's span. Beyond the breakdown point, the LEV expands in size and the flow within the vortex core is highly unsteady. During the downstroke, the increased LEV circulation for non-zero advance ratios was found to cause the LEV to break down earlier along the wing's span. This created a burst LEV structure that closely resembled the LEV from the lower Reynolds number, except that the flow was now unsteady due to the LEV breakdown. At high advance ratios and high aspect ratios, the burst LEV was shed from the wing, resulting in a region of highly unsteady separated flow being developed on the wing. Thus, a similar dependence of the LEV stability on the advance ratio and aspect ratio was observed at this Reynolds number, except that the growth of the LEV is through vortex breakdown rather than viscous diffusion. Hence the findings of this study are likely to apply across a wide range of Reynolds numbers.

Acknowledgement

This research was undertaken with the assistance of resources provided at the Australian National University through the National Computational Merit Allocation Scheme supported by the Australian Government.

Supplementary movies

Supplementary movies are available at <http://dx.doi.org/10.1017/jfm.2014.262>.

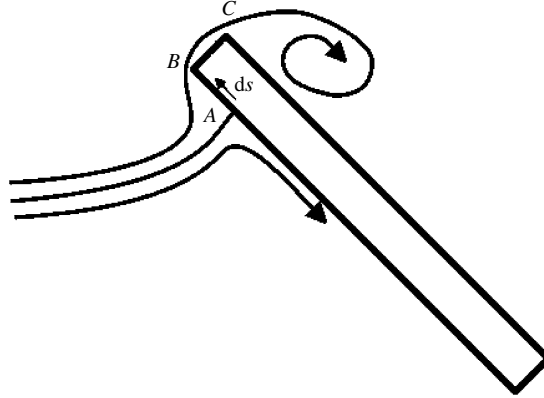


FIGURE 24. Schematic of a typical two-dimensional streamline pattern at one point along the wing's span.

Appendix A. Vorticity generation

Vorticity is generated at the boundary between a body's surface and the fluid. The flux of vorticity from these boundaries, as reported by Morton (1984), is given by

$$-\nu(\mathbf{n} \cdot \nabla \boldsymbol{\omega}) = -\rho^{-1}(\mathbf{n} \times \nabla)p - \mathbf{n} \times \mathbf{a}, \quad (\text{A } 1)$$

where ν is the kinematic viscosity, \mathbf{n} is the wall unit normal vector, $\boldsymbol{\omega}$ is the vorticity vector and \mathbf{a} is the acceleration vector of the boundary. This equation is evaluated at the surface and shows that vorticity is generated from tangential pressure gradients and the tangential acceleration of the boundary (Morton 1984).

We used (A 1) to estimate the vorticity being generated at one spanwise location on the wing's surface for our flapping wing simulations. Figure 24 presents a schematic of a typical two-dimensional streamline pattern of the flow around a flapping wing. The flow stagnates on the wing's lower surface at A. The fluid above A flows over the leading edge, while the fluid below A travels along the underside of the wing. Therefore, any vorticity that is generated between A and C is advected over the leading edge and into the LEV. By integrating (A 1) along the wing's surface from A to C, the time rate of change of LEV circulation per unit span can be calculated that is due to the generation of vorticity. This results in

$$\frac{d\Gamma_z}{dt} = \rho^{-1} \int_A^C \frac{\partial p}{\partial s} ds + \int_A^B \frac{dU_i}{dt} \sin(|\alpha_i|) ds - \int_B^C \frac{dU_i}{dt} \cos(|\alpha_i|) ds. \quad (\text{A } 2)$$

The first term on the right-hand side of (A 2) is the vorticity generation due to the pressure gradient, and the other two terms account for the vorticity generation due to the tangential acceleration of the wing's bottom surface and leading edge, respectively. As we are primarily interested in the generation of vorticity outside of the stroke reversal, the acceleration of the wing's surface due to the pitch rotation of the wing has been neglected. The acceleration of each point on the wing's surface can therefore be approximated as the time rate of change of the relative velocity at that spanwise location (i.e. $\mathbf{a} = d\mathbf{U}_i/dt$). As the wing's acceleration is in the x -direction, this needs to be modified to calculate the component that acts tangentially to each surface. Hence the use of $\sin(|\alpha_i|)$ and $\cos(|\alpha_i|)$ in (A 2), where α_i is given by (2.7). Equation (A 2)

has been written for the downstroke and in terms of the coordinate system shown in figure 1. Therefore a negative pressure gradient results in the generation of negative vorticity, and a positive time rate of change of U_i causes positive vorticity to be generated on the wing's bottom surface and negative vorticity to be generated on the leading edge. For the upstroke this description of vorticity generation is reversed, owing to the change in orientation of the wing, and therefore the time rate of change of circulation is the negative of (A2).

Equation (A2) was evaluated at 25% span for the downstroke, and the results are presented in figure 10, where figure 10(a) is the computed value of the pressure gradient term and figure 10(b) is the sum of the acceleration terms.

REFERENCES

- AONO, H., LIANG, F. & LIU, H. 2008 Near- and far-field aerodynamics in insect hovering flight: an integrated computational study. *J. Expl Biol.* **211**, 239–257.
- BEEM, H. R., RIVAL, D. E. & TRIANTAFYLLOU, M. S. 2012 On the stabilization of leading-edge vortices with spanwise flow. *Exp. Fluids* **52** (2), 511–517.
- VAN DEN BERG, C. & ELLINGTON, C. P. 1997 The three-dimensional leading-edge vortex of a 'hovering' model hawkmoth. *Phil. Trans. R. Soc. B* **352** (1351), 329–340.
- BIRCH, J. M. & DICKINSON, M. H. 2001 Spanwise flow and the attachment of the leading-edge vortex on insect wings. *Nature* **412**, 729–733.
- BIRCH, J. M., DICKSON, W. B. & DICKINSON, M. H. 2004 Force production and flow structure of the leading edge vortex on flapping wings at high and low Reynolds numbers. *J. Expl Biol.* **207** (7), 1063–1072.
- BROSS, M., OZEN, C. A. & ROCKWELL, D. 2013 Flow structure on a rotating wing: effect of steady incident flow. *Phys. Fluids* **25** (8), 081901.
- CHENG, B., SANE, S. P., BARBERA, G., TROOLIN, D. R., STRAND, T. & DENG, X. 2013 Three-dimensional flow visualization and vorticity dynamics in revolving wings. *Exp. Fluids* **54** (1), XXX–XXX.
- DICKINSON, M. H. & GOTZ, K. G. 1993 Unsteady aerodynamic performance of model wings at low Reynolds numbers. *J. Expl Biol.* **174** (1), 45–65.
- DICKINSON, M. H., LEHMANN, F.-O. & SANE, S. P. 1999 Wing rotation and the aerodynamic basis of insect flight. *Science* **284** (5422), 1954–1960.
- DICKSON, W. B. & DICKINSON, M. H. 2004 The effect of advance ratio on the aerodynamics of revolving wings. *J. Expl Biol.* **207** (24), 4269–4281.
- DUDLEY, R. & ELLINGTON, C. P. 1990 Mechanics of forward flight in bumblebees. I. Kinematics and morphology. *J. Expl Biol.* **148**, 19–52.
- ELLINGTON, C. P. 1984a The aerodynamics of hovering insect flight. II. Morphological parameters. *Phil. Trans. R. Soc. B* **305** (1122), 17–40.
- ELLINGTON, C. P. 1984b The aerodynamics of hovering insect flight. III. Kinematics. *Phil. Trans. R. Soc. B* **305** (1122), 41–78.
- ELLINGTON, C. P. 1999 The novel aerodynamics of insect flight: applications to micro-air vehicles. *J. Expl Biol.* **202**, 3439–3448.
- ELLINGTON, C. P., VAN DEN BERG, C., WILLMOTT, A. P. & THOMAS, A. L. R. 1996 Leading-edge vortices in insect flight. *Nature* **384** (19), 626–630.
- FRY, S. N., SAYAMAN, R. & DICKINSON, M. H. 2005 The aerodynamics of hovering flight in *Drosophila*. *J. Expl Biol.* **208**, 2303–2318.
- GOPALAKRISHNAN, P. & TAFTI, D. K. 2010 Effect of wing flexibility on lift and thrust production in flapping flight. *AIAA J.* **48** (5), 865–877.
- HALL, M. G. 1972 Vortex breakdown. *Annu. Rev. Fluid Mech.* **4** (1), 195–218.
- HARBIG, R. R., SHERIDAN, J. & THOMPSON, M. C. 2013 Reynolds number and aspect ratio effects on the leading-edge vortex for rotating insect wing planforms. *J. Fluid Mech.* **717**, 166–192.

- HUNT, J. C. R., WRAY, A. A. & MOIN, P. 1988 Eddies, streams, and convergence zones in turbulent flows. *Tech. Rep.* CTR-S88. Center for Turbulence Research.
- JARDIN, T., FARCY, A. & DAVID, L. 2012 Three-dimensional effects in hovering flapping flight. *J. Fluid Mech.* **702**, 102–125.
- LEIBOVICH, S. 1978 The structure of vortex breakdown. *Annu. Rev. Fluid Mech.* **10**, 221–246.
- LENTINK, D. & DICKINSON, M. H. 2009 Rotational accelerations stabilize leading edge vortices on revolving fly wings. *J. Expl Biol.* **212** (16), 2705–2719.
- LIU, H. & AONO, H. 2009 Size effects on insect hovering aerodynamics: an integrated computational study. *Bioinspir. Biomim.* **4**, 015002.
- LU, Y., SHEN, G. X. & LAI, G. J. 2006 Dual leading-edge vortices on flapping wings. *J. Expl Biol.* **209**, 5005–5016.
- MAXWORTHY, T. 1979 Experiments on the Weis-Fogh mechanism of lift generation by insects in hovering flight. Part 1. Dynamics of the ‘fling’. *J. Fluid Mech.* **93** (1), 47–63.
- MORTON, B. R. 1984 The generation and decay of vorticity. *Geophys. Astrophys. Fluid Dyn.* **28** (3), 277–308.
- NAGAI, H., ISOGAI, K., FUJIMOTO, T. & HAYASE, T. 2009 Experimental and numerical study of forward flight aerodynamics of insect flapping wing. *AIAA J.* **47** (3), 730–742.
- POELMA, C., DICKSON, W. B. & DICKINSON, M. H. 2006 Time-resolved reconstruction of the full velocity field around a dynamically-scaled flapping wing. *Exp. Fluids* **41** (2), 213–225.
- RIVAL, D. E. & WONG, J. G. 2013 Measurements of vortex stretching on two-dimensional rotating plates with varying sweep. In *Proceedings of the 10th International Symposium on Particle Image Velocimetry, Delft, The Netherlands, July 1–3, 2013*.
- ROACHE, P. J. 1998 Verification of codes and calculations. *AIAA J.* **36** (5), 696–702.
- SANE, S. P. 2003 The aerodynamics of insect flight. *J. Expl Biol.* **206**, 4191–4208.
- SANE, S. P. & DICKINSON, M. H. 2001 The control of flight force by a flapping wing: lift and drag production. *J. Expl Biol.* **204**, 2607–2626.
- SHYY, W., AONO, H., CHIMAKURTHI, S. K., TRIZILA, P., KANG, C. K., CESNIK, C. E. S. & LIU, H. 2010 Recent progress in flapping wing aerodynamics and aeroelasticity. *Prog. Aerosp. Sci.* **46** (7), 284–327.
- SUN, M. 2003 Aerodynamic force generation and power requirements in forward flight in a fruit fly with modelled wing motion. *J. Expl Biol.* **206** (17), 3065–3083.
- USHERWOOD, J. R. & ELLINGTON, C. P. 2002 The aerodynamics of revolving wings I. Model hawkmoth wings. *J. Expl Biol.* **205** (11), 1547–1564.
- VENKATA, S. K. & JONES, A. R. 2013 Leading-edge vortex structure over multiple revolutions of a rotating wing. *J. Aircraft* **50** (4), 1312–1316.
- WANG, Z. J. 2005 Dissecting insect flight. *Annu. Rev. Fluid Mech.* **37**, 183–210.
- WANG, Z. J. 2008 Aerodynamic efficiency of flapping flight: analysis of a two-stroke model. *J. Expl Biol.* **211** (2), 234–238.
- WEIS-FOGH, T. 1973 Quick estimates of flight fitness in hovering animals, including novel mechanisms for lift production. *J. Expl Biol.* **59**, 169–230.
- WILLMOTT, A. P. & ELLINGTON, C. P. 1997 The mechanics of flight in the hawkmoth *Manduca sexta*. I. Kinematics of hovering and forward flight. *J. Expl Biol.* **200**, 2705–2722.
- WONG, J. G., KRIEGSEIS, J. & RIVAL, D. E. 2013 An investigation into vortex growth and stabilization for two-dimensional plunging and flapping plates with varying sweep. *J. Fluids Struct.* **43**, 231–243.
- ZANKER, J. M. 1990 The wing beat of *Drosophila melanogaster*. I. Kinematics. *Phil. Trans. R. Soc. B* **327** (1238), 1–18.